Mechanical (and Materials) Engineering -- Dissertations, Theses, and Student Research

Mechanical & Materials Engineering, Department of

Spring 4-27-2015

Microstructure and Phase Analysis in Mn-Al and Zr-Co Permanent Magnets

Michael J. Lucis
University of Nebraska-Lincoln, mlucis@huskers.unl.edu

Microstructure and Phase Analysis in Mn-Al and Zr-Co Permanent Magnets

by

Michael J. Lucis

A DISSERTATION

Presented to the Faculty of

The Graduate College at the University of Nebraska

In Partial Fulfilment of Requirements

For the Degree of Doctor of Philosophy

Major: Engineering (Materials Engineering)

Under the Supervision of Professor Jeffrey E. Shield

Lincoln, Nebraska

April, 2015

Microstructure and Phase Analysis in Mn-Al and Zr-Co Permanent Magnets

Michael J. Lucis, Ph.D.

University of Nebraska, 2015

Adviser: Jeffrey E. Shield

In America's search for energy independence, the development of rare-earth free permanent magnets is one hurdle that still stands in the way. Permanent magnet motors provide a higher efficiency than induction motors in applications such as hybrid vehicles and wind turbines. This thesis investigates the ability of two materials, Mn-Al and Zr-Co, to fill this need for a permanent magnet material whose components are readily available within the U.S. and whose supply chain is more stable than that of the rare-earth materials. This thesis focuses on the creation and optimization of these two materials to later be used as the hard phase in nanocomposites with high energy products (greater than 10 MGOe).

Mn-Al is capable of forming the pure $L1_0$ structure at a composition of $Mn_{54}Al_{43}C_3$. When Mn is replaced by Fe or Cu using the formula $Mn_{48}Al_{43}C_3T_6$ the anisotropy constant is lowered from $1.3 \cdot 10^7$ ergs/cm^3 to $1.0 \cdot 10^7$ ergs/cm^3 and $0.8 \cdot 10^7$ ergs/cm^3 respectively. Previous studies have reported a loss in magnetization in Mn-Al alloys during mechanical milling. The reason for this loss in magnetization was investigated and found to be due to the formation of the equilibrium β-Mn phase of the composition Mn_3Al_2 and not due to oxidation or site disorder. It was also shown that fully dense Mn-Al permanent magnets can be created at hot pressing temperatures at or above 700°C and that the ε-phase to τ-phase transition and consolidation can be combined into a single processing step. The addition of small amounts of Cu to the alloy, 3% atomic, can increase the compaction density allowing high densities to be achieved at lower pressing temperatures.

While the structure is still under debate, alloys at the composition Zr_2Co_{11} in the Zr-Co system have been shown to have hard magnetic properties. This thesis shows that multiple structures exist at this Zr_2Co_{11} composition and that altering the cooling rate during solidification of the alloy affects the ratio of the phase composition and therefore affects the magnetic properties. Phase diagrams for the Zr-Co system show that the Zr_2Co_{11} phase is stable to a temperature of 1272^oC, at which point the Zr_6Co_{23} phase is the most favorable. However, this thesis shows that the Zr_6Co_{23} phase forms at room temperature during high energy mechanical milling and at annealing temperatures as low as 600^oC. Since high energy mechanical milling was not a potential method to creating single crystalline particles, hydrogen embrittlement was investigated. Hydrochloric acid was used to induce hydrogen embrittlement in the Zr_2Co_{11} alloy, modifying the fracture characteristics of the alloy causing it to occur primarily along grain boundaries resulting in single crystalline particles with remanent magnetization enhancement.

Acknowledgements

First I would like to thank my adviser Dr. Jeffrey Shield. Dr. Shield was more than just an academic adviser and mentor but a role model of not just of a scientist but of a professional and a person. I was truly lucky to be able to spend my graduate career under his guidance. I would also like to take a moment to thank Dr. Kevin Cole and Dr. David Allen for introducing me to the research field during my undergraduate work, without their encouragement I would never have considered pursuing a PhD and a career in research.

I would like to thank Dr. Merhdad Negahban for is guidance in the exchange program that allowed me to attend the University of Rouen as part of my studies. I would like to thank the staff at the University of Rouen: Dr. Jean-Marc Saiter, Dr. Jean-Marie LeBreton, Emeric Folcke, Julien Bran, and Malick Jean, for their assistance and for accepting me into their research group.

I would like to thank Dr. David Sellmyer for his collaboration and access to his lab to perform magnetic measurements. I would also like to thank Dr. Ralph Skomski, Dr. Steven Michalski, Dr. Shah Valloppilly, and Dr. Xingzhong Li for their guidance and assistance with lab equipment and NCMN facilities.

A special thanks to Dr. Shield, Dr. Negahban, Dr. Skomski, and Dr. Joseph Turner for serving on my advisory committee and for their guidance and support.

I would also like to thank my research group mates: Farhad Golkar, Jay Jayaraman, Jordie Bornhoft, Mak Koten, Meiyu Wang, Yunlong Geng, Pinaki Mukherjee, Hellen Jiang, Damon Tian, and Jake Lewis. Thank you for support, I know this would not have been possible, or nearly as enjoyable, without our discussions in the office both on work and our lives outside of work.

Finally I would like to thank my parents, Dan and Karen Lucis. They supported through all of my health issues, even when I had given up hope. Without their support I would never have been able to achieve something like this. I would also like to thank the rest of my family and friends for their support.

GRANT INFORMATION

Contents

IX

I. Introduction

1. Motivation

Permanent magnets have received significant attention over the last century. The first permanent magnet discovered was naturally occurring magnetite, Fe_3O_4, originally used in compasses [1]. In the 20th century the number of applications for permanent magnets expanded dramatically and a need for stronger, higher energy materials began. Permanent magnets today have generated even larger amounts of interest due to the move towards renewable clean energy sources. A critical component to the efficiency of these renewable energy sources is the motor that converts between the mechanical power and electrical energy. It has been shown that the permanent magnet motors are more efficient than induction motors in applications where weight and volume are a concern [2]. A 2009 study showed permanent magnet motors can reduce the space used by 70% and the weight of the motor by 60% compared to typical induction motors in 5 horsepower applications [3]. The application of permanent magnet motors in this way has created new challenges. It is no longer just about maximizing energy product, but doing it with materials that can be produced on a massive scale. Previously, the leading applications for rare-earth permanent magnets included hard disc drives, speakers, DVD/CD ROM, cordless tools, and mobile phones [2]. These applications require small amounts of the magnetic material for relatively small power outputs. The supply of rare-earth materials was easily able to meet the demand for these applications, but new applications, such as wind turbines and electric vehicles, require much larger quantities than these previous applications, causing rare-earth prices to rise and China to limit exportation of these materials [1]. This has sparked research interest in

materials that had previously been abandoned in favor of the more effective rare earth materials. The development and improvement of these rare earth free materials could lead to their use in some of these applications, returning the use of rare earth magnets to only applications where their high energy products are truly needed, therefore reducing the stress on their supply. The development of these materials, as well as possible future replacement materials, will be discussed in section 3. In the next section we will discuss the basics of magnetism that will be essential to quantifying the performance of these magnetic materials.

2. Magnetism

i. Types of Magnetism

Magnetic fields result from the motion of electrons. As electrons rotate they create a magnetic field perpendicular to the plane of motion (figure 1.1). Magnetic fields can be a result of either the electrons spin or the electrons orbit around the nucleus.
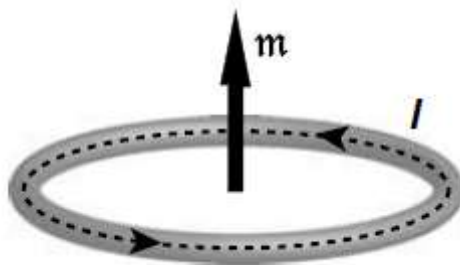
Figure 1.1: Magnetic moment

Magnetic moments arise from electron motion. Both the electrons spin and orbit create a magnetic field. From [4].

Depending on the arrangement of the moments from the individual electrons within a material, many different types of magnetism are possible, four examples are: ferromagnetism, antiferromagnetism, paramagnetism, and diamagnetism. Ferromagnetism is the most useful of the different types of magnetism for permanent magnets and the one on which this

research is focused. Ferromagnetism occurs when the magnetic moments of the atoms align

in the same direction as shown in figure 1.2.
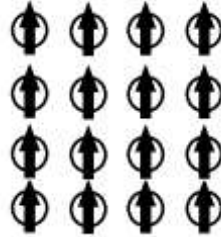
Figure 1.2: Ferromagnetic moment alignment

Ferromagnetism only occurs naturally in a select few elements. The four elements with naturally

occurring ferromagnetism at room temperature are iron, cobalt, gadolinium, and nickel. The

magnetism in these materials is controlled by the exchange interaction between the spin

moments of the atoms. This interaction is dependent on the distance between the atoms, which

in turn affects the density of states causing the material to act in either a ferromagnetic or

antiferromagnetic manner. The Bethe-Slater curve (figure 1.3) shows the exchange integral, J, as

a function of the interatomic radius. There is a minimum radius where ferromagnetic exchange

can occur, and if the atoms are too close together antiferromagnetic exchange occurs.

Antiferromagnetism occurs when the density of states in a metal is not high enough and the

atoms couple in an anti-parallel direction instead [4]. This curve is partially applicable to Mn-Al

where the unusual ferromagnetic exchange is encountered in the dense-packed Mn planes [35].

4
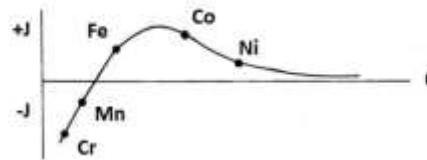
Figure I-1: The Bethe-Slater curve

The Bethe-Slater curve shows the effect of interatomic radius on the exchange integral "J".

When "J" is positive ferromagnetism occurs, when it is negative the material is

antiferromagnetic.

There are multiple types of antiferromagnetism, the two most common are layered antiferromagnetism and checkerboard antiferromagnetism. Layered antiferromagnetism (figure I-4a) is when the spin alternates based on the layer in the crystal structure. In checkerboard antiferromagnetism the atoms are surrounded by opposite spins in all crystallographic directions (figure I-4b).

Figure 1.2a: Layered antiferromagnetism Figure 1.4b: checkerboard antiferromagnetism

Antiferromagnetism results in a zero net magnetization, as each spin is balanced by one in the opposite direction.

Similar to antiferromagnetism is a type of magnetism known as ferrimagnetism. Ferrimagnetism is only possible in compounds with multiple types of atoms, or in compounds with differing lattice sites such as Fe_3O_4. In ferrimagnetic materials the atoms are aligned antiparallel but due to the fact that there exists two different types of atoms, and therefore two magnetic moments with two different magnitudes, the net magnetic moment does not sum to zero. Figure 1.5 shows an example where the total magnetic moment would be equal to the sum of the moments of "A" atoms minus the sum of the moments of "B" atoms.
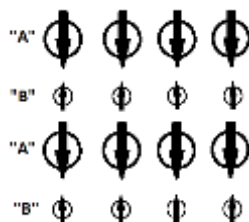
Figure 1.5: Ferrimagnetism

Ferrimagnetism is where differing atoms aligned in an antiparallel order result in an overall moment in one direction.

The third type of magnetism is paramagnetism. Curie-Weiss Paramagnetism occurs when the thermal vibration energy of the material is strong enough to overcome the magnetic coupling; at lower temperatures the material can revert to either ferromagnetic or antiferromagnetic behavior. When Paramagnetism occurs, the magnetic moments point in random directions (figure 1.6). This results in an overall magnetic moment of zero when the material is not under the influence of an external magnetic field. Under the influence of a magnetic field, the atomic moments begin to align with the field and result in a net magnetization. The rate that magnetization increases with an increasing field is called the magnetic susceptibility, χ. The

increase of the magnetization, M, is linear in relation to the applied field, H, resulting in the

defining equation: $\chi=M/H$.

Figure 1.6: Paramagnetism

Paramagnetism is where the atomic moments constantly change their alignment in random directions.

The temperature at which these thermal effects are strong enough to overcome the preference for

the magnetic moments to align is called the Curie temperature. Experimentally the Curie

temperature can be found by measuring the spontaneous magnetization of a material at

increasing temperatures until the magnetization reaches zero. An example of this curve is shown

for nickel in figure 1.7.
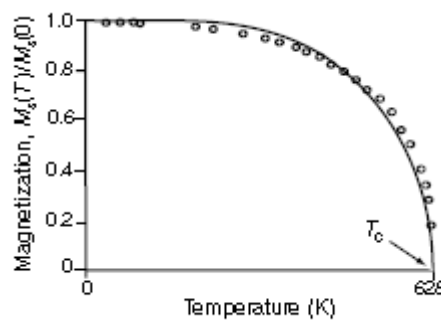
Figure 1.7: Experimental determination of nickel's Curie temperature.

From [4].

As can be seen in figure 1.7, the ferromagnetic properties follow a power law behavior. Even

when the applied temperature is below the Curie temperature of the material, if the working

temperature approaches the Curie temperature the magnetic material properties will decrease dramatically.

The final type of magnetism is diamagnetism. Diamagnetism is a result of the orbital moment from the valence shell of electrons. All materials possess diamagnetism; however, the diamagnetic susceptibilities are small compared to that of other types of magnetism and so are only apparent in materials where the spin contribution to the magnetism is not dominant. The molar susceptibilities of diamagnetic moments range from $(-10)^{-8}$ to $(-10)^{-11}$ [4].

ii. The Magnetic Hysteresis Loop

The magnetic measurement used in this thesis is the magnetic hysteresis loop. From this curve, the B-H curve can be obtained that will be used to find the maximum energy product of the material. "H" is defined as the magnetic field. "B" is known as the magnetic induction. The two are related by taking into account the field present inside the material. The resulting equation is $B = \mu_0(H+M)$ where μ is the permeability and M is the magnetization of the material. Figure 1.8 shows a depiction of the difference between the "H" field and the "B" field.
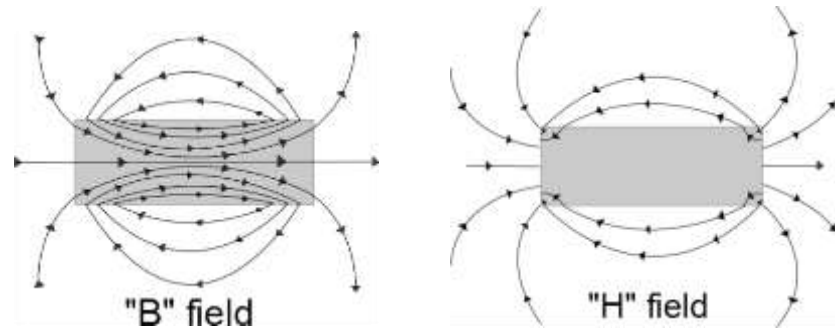
Figure 1.8: "B" field and "H" field.

The magnetic induction field "B", shown on the left, is a combination of the "H" field and

the magnetization "M" of the material. The "H" field is the measured field and shown on

the right.

There are multiple important values obtained from the M-H hysteresis loop that will be used to

quantify the material. Figure 1.9 shows an M-H hysteresis loop with these values labeled. The

first is the saturation magnetization, or the highest magnetization for the material (point "A" in

figure1.9). This is where we will begin measuring the hysteresis loop, fully magnetizing the

material in one direction. As we begin to decrease the magnetization, the next important value is

the remanent magnetization (point "B" in figure 1.9). This is the value of the magnetization at

zero applied field, after the material has been magnetized. As a field in the opposite direction is

applied, the magnetization is reduced until it reaches zero. The field that causes the material to

return to zero is called the coercivity (point "C" in figure 1.9). In the M-H loop this is known as

the intrinsic coercivity, H_{ci}. As the field continues to increase in the opposite direction, the

magnetization decreases until the material is saturated in the opposite direction, point "D" in

figure 1.9. Later in this section, we will see that the figure of merit for permanent magnet materials occurs within the second quadrant, making the remanent magnetization and coercivity important values when quantifying these materials.
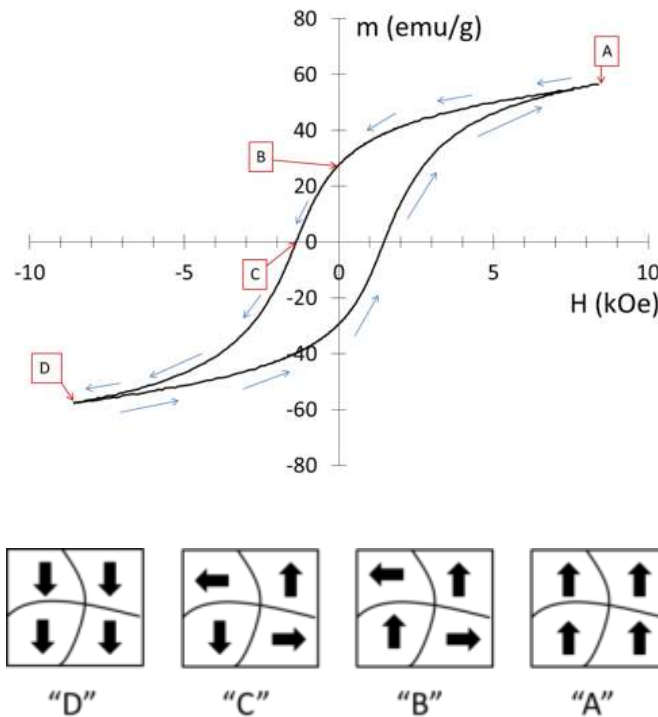
Figure 1.9: Magnetic Hysteresis Loop

In the hysteresis loop points "A" and "D" represent the fully saturated material. Point "B" is called the remanence magnetization and "C" is known as the intrinsic coercivity.

If the field is not large enough to saturate the material, the loop is a minor loop. In a minor loop the values for saturation magnetization, remanence magnetization, and coercivity will be different from those obtained in a major loop. In this thesis, there will be examples where the materials are fully saturated to begin with but during the measurement the material is not able to

be fully saturated in the opposite direction, resulting in a non-symmetric loop; an example of this is shown in figure I-12.
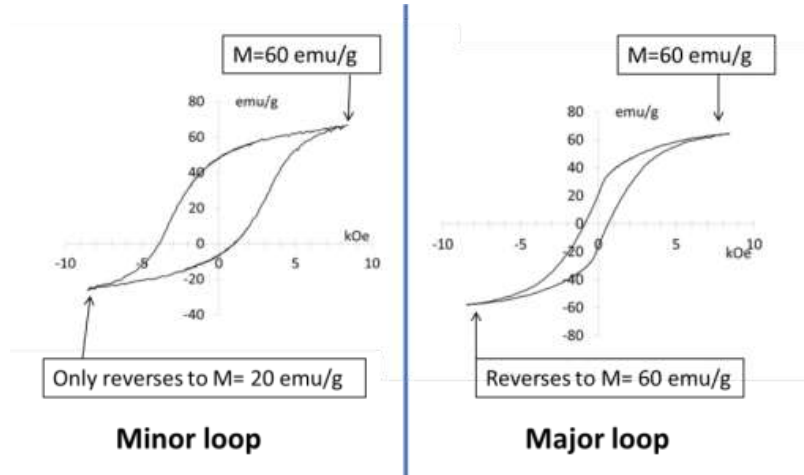
Figure 1.10: Major and Minor Loops

In minor loops the field is not high enough to fully reverse the material, resulting in a lower magnetization in the opposite direction and what appears to be an unbalanced loop.

Although the M-H loop is commonly presented, the maximum energy product, which is the figure of merit for permanent magnet materials, is obtained from the B-H loop. As previously mentioned the magnetic induction "B" can be found using the formula $B=\mu(M+H)$. Similar to remanence in the M-H loop, the remaining induction in zero field is referred to as the remanent induction or "B_r" (figure 1.11). The maximum energy product "$(BH)_{max}$" is found by multiplying the induction "B" and the field "H" in the second quadrant. The field where the "$(BH)_{max}$" occurs is known as the loading field or "H_d". An example of the B-H loop can be seen in figure 1.11 with these values labeled.
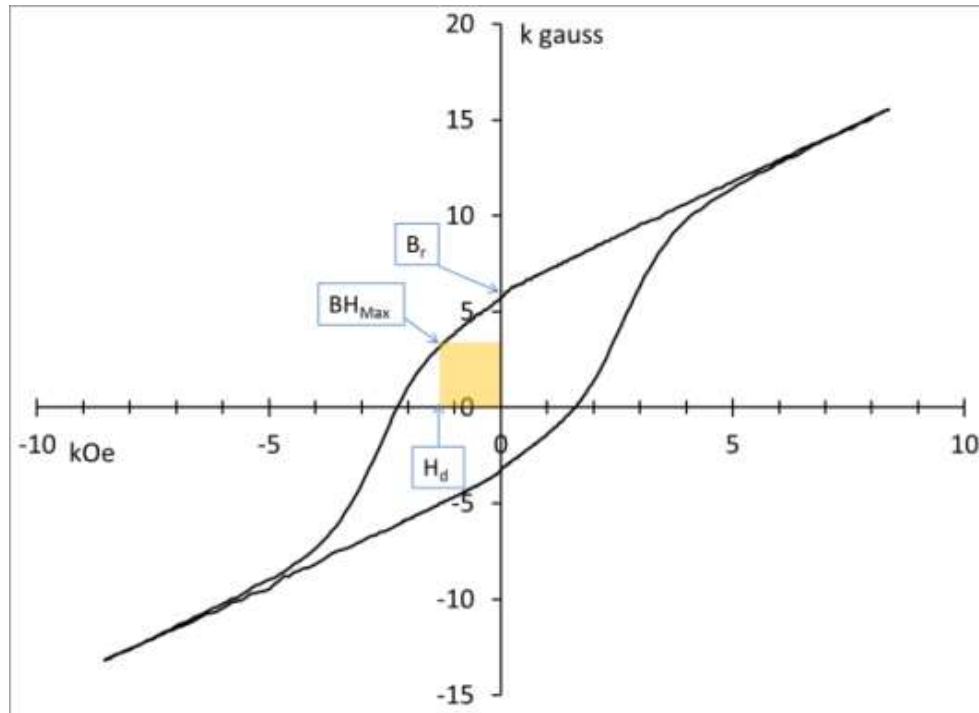
Figure 1.11: BH Loop

The BH loop is where the maximum energy product can be measured, which is the figure of merit for permanent magnet materials.

3. Magnetic Materials and Controlling their Properties

i. Intrinsic Properties

There are two types of material properties: intrinsic and extrinsic. Intrinsic properties are controlled by the crystal structure and chemical composition of the material. Extrinsic properties are affected by the material's microstructure. Examples of intrinsic properties include Curie temperature, saturation magnetization, and magnetocrystalline anisotropy. Anisotropy depends on the crystal symmetry and is a measure of the variation of the magnetization process along different crystallographic directions. For permanent magnet applications uniaxial anisotropy is preferred because there are no intermediate easy axes in the reversal process. In applications it is important to maintain the magnetization in the chosen direction in as strong of a reverse field as

possible; maintaining uniaxial anisotropy aids this effort. Figure 1.12 demonstrates the difference between multi-axis and uniaxial anisotropy reversal.
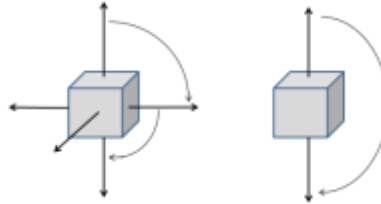
Figure 1.12: Easy Axis reversal. When a sample has more than one easy axis, the high symmetry allows for easy reversal of the magnetic moment

ii. Extrinsic Properties

Extrinsic properties are properties that are affected by the material's microstructure. Examples of extrinsic properties include the material's coercivity and the remanent magnetization. The coercivity of a material is highly dependent on the grain size. To understand this dependence we must first introduce the concept of magnetic domains. Magnetic domains are areas of similar magnetic alignment used to minimize the total magnetostatic energy of the system. This domain structure is a result of the anisotropy discussed earlier. In order to minimize the magnetostatic energy, grains, which consist of a single crystal, are divided by domain walls that separate different magnetic alignments within the crystal. These domains must be aligned along the easy axes. The lack of intermediate easy axes is another one of the benefits of uniaxial anisotropy (figure 1.13).
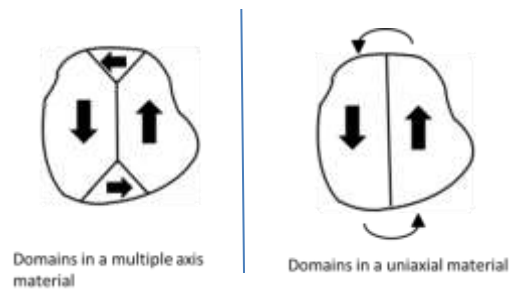
Figure 1.13: Domain structures

When there is uniaxial anisotropy, the domains at 90° to complete the field within the material, cannot exist since there is only one easy axis.

The formation of these domain walls is the reason for the dependence of the coercivity on the grain size. As the grains become smaller the volume magnetization decreases, reducing the total magnetic energy of the grain and therefore reducing the energy benefit for the creation of the domain. If the magnetization contained within this grain becomes small enough, the energy associated with the domain wall becomes more than the reduction in magnetostatic energy resulting from the creation of the domain. At this point the grain does not create domains and is a single domain particle. This critical size is known as the single domain limit, and varies based on the material. The single domain limit is given by [4] where the critical radius (R_{sd}) is a function of the domain wall constants A and K_{1c}, the permeability of free space (μ_0), and saturation magnetization (M_s) (equation 1):

$$R_{sd} \approx 9\sqrt{AK_{1c}}/\mu_0 M_s^2 \qquad (1)$$
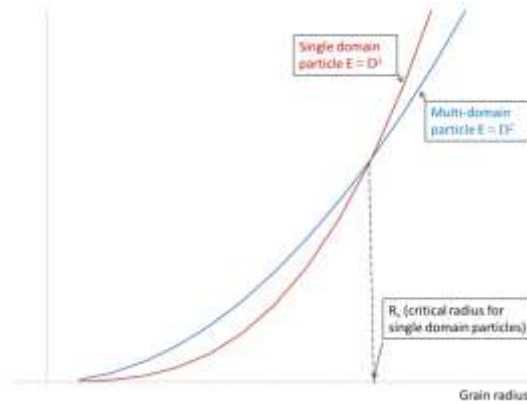
Figure 1.14: Energy of single and multi-domain particles

The energy of a single domain grain is related to the cube of the grain diameter, the energy of a multi-domain particle is related to the square of the grain diameter. This results in a critical value where the single domain particle becomes more energy favorable.

The superparamagnetic limit, D_P in figure 1.15, occurs when the grains of a material become so small that the material begins to act like a paramagnetic material. If we recall paramagnetism occurs because the thermal energy over powers the alignment of the magnetic moment of the material. As grains get continually smaller in the nanoscale range, exchange effects between grains dominate causing random anisotropy. A plot of coercivity as a function of grain size is shown in figure 1.15.
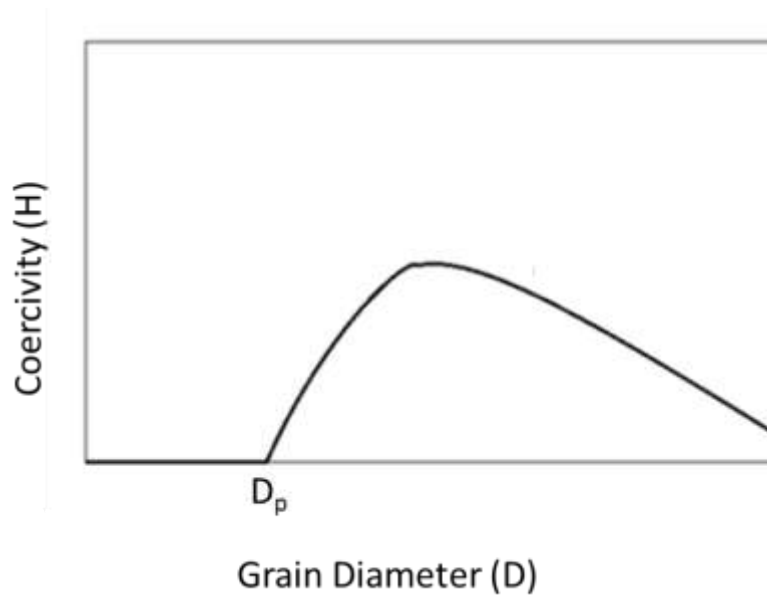
Figure 1.15: Coercivity as it relates to grain size

After the single domain limit, the coercivity decreases until the material becomes

paramagnetic due to random anisotropy (D_p).

Another factor that affects the coercivity of a material is the magnetic coupling between grains. Previously figure 1.8 showed the field lines generate by a magnet, a bulk magnet can be modeled as a collection of these individual magnetic particles. In this case the fields generated by neighboring grains create a field in the opposite direction of the magnetization of the grains. These fields decrease the applied field needed to reverse the magnetization (figure 1.16). As the neighboring grains are moved closer together, the strength of the magnetostatic interaction increases. When a second phase is introduced between these grains, it also prevents grains from causing reversal in neighboring grains.
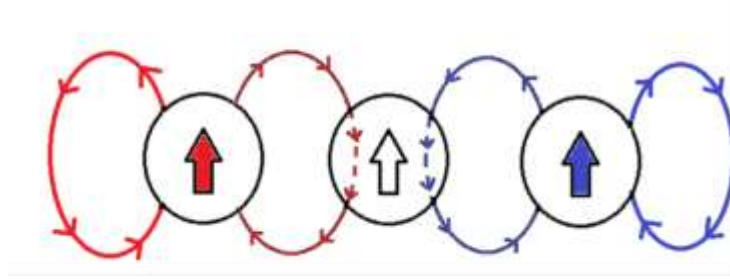
Figure 1.16: Magnetostatic Interactions

Magnetostatic interactions contribute to the reversal field, lowering the required external field to cause reversal of the magnetic moment.

The remanent magnetization is also an extrinsic property; however it is not affected directly by the grain size. Instead remanent magnetization is affected by the alignment of the easy axis of the grains. The Stoner-Wohlfarth model is an analytical model that describes the ideal hysteretic behavior of non-interacting uniaxial particles. This model shows that when a small particle of a uniaxial material undergoes demagnetization in a field aligned with the easy axis that the hysteresis loop will be square. If the field is applied at 90° to the easy axis, it will instead be a line that passes through the origin. In reality, a magnetic material will show a behavior somewhere between the two. A multi-grain material with no alignment will behave like a Stoner-Wohlfarth particle in a 45° field (figure 1.17).
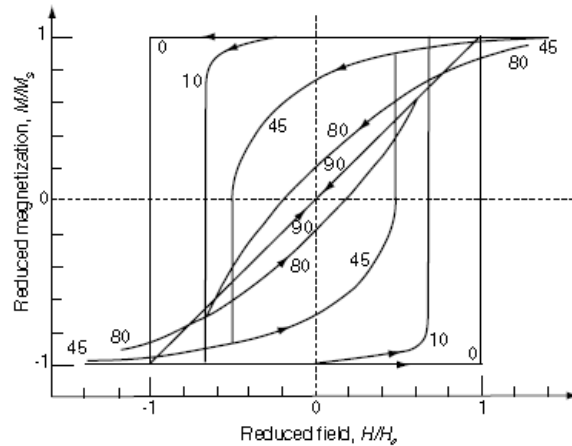
Figure 1.17: Stoner-Wohlfarth Particles

From [4]

The effect of this alignment on remanence, coercivity, and demagnetization curve shape is important in permanent magnetic materials. Recall that the energy product is an area found in the second quadrant. Controlling the material properties is important but in order to maximize the energy product the material must be aligned into an anisotropic magnet.

The final microstructural affect that will be discussed is exchange coupling. Exchange coupling is a phenomenon that occurs between neighboring magnetic grains across grain boundaries that allow the grains to act as coupled crystallites rather than superparamagnetic particles [4]. Exchange coupling can also occur between two different magnetic materials that are combined in a nanocomposite in order to increase the energy product. Soft magnetic materials refer to materials with low coercivity and generally high magnetizations. Hard magnetic materials have high coercivity but generally do not have as high of magnetization values. Exchange coupling attempts to combine the best of both materials to increase the energy product of the material (figure 1.18). If a material is effectively exchange coupled, the coercivity is less than that of the hard phase material due to a reduced anisotropy constant; however the

saturation magnetization of the material follows a rule of mixtures for the various phase fractions and magnetizations, $M_{nanocomposite} = X_A \cdot M_A + X_B \cdot M_B$. This increase in magnetization is enough to make exchange coupling an effective way of increasing the energy product.
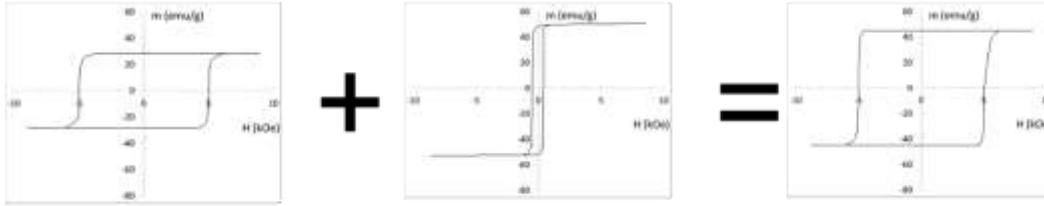
Figure 1.18: Hard, Soft, and Exchanged Coupled Hysteresis loops

In order for a material to be successfully exchange coupled, the phases must have a nanoscale structure. In order for successful exchange coupling, the diameter of the soft phase must be less than twice the domain wall width of the hard phase [4]. The thickness of the domain wall, δ_w, is described by the equation 2, where A is the exchange stiffness between the domains and K is the anisotropy constant.

$$\delta_w = \pi \sqrt{\frac{A}{K}} \qquad\qquad (2)$$

This couples the magnetic moment of the soft phase to the neighboring hard phase, preventing it from reversing before the hard phase material does, see figure 1.19.
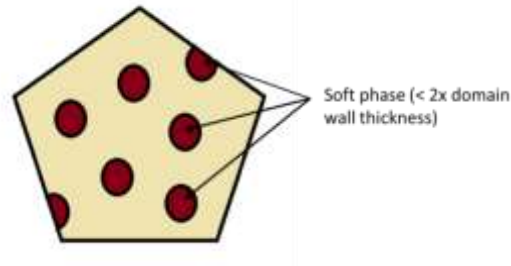
Figure 1.19: Exchange Coupling Structure

If the material is not successfully exchange coupled the material demonstrates two-phase reversal behavior. In the hysteresis loop the soft phase reverse first at its lower coercivity separate from the hard magnetic phase. Figure 1.20 shows an experimental example of this. In hysteresis loop "a", the soft phase particles are 4 nm and below the limit for exchange coupling. In hysteresis loop "b" the soft phase particles are 12 nm and are too large to successfully exchange couple.
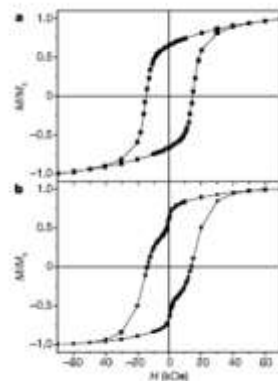
"a": 4 nm soft phase particles

"b": 12 nm soft phase particles

Figure 1.20: Experimental Exchange Coupling

In loop "a" the 4 nm particles are small enough to effective exchange couple and the loop appears single phase. In loop "b" the particles are too large and reverse before the hard phase. From [5]

4. Permanent Magnet Materials

i. Rare- Earth Permanent Magnets

Today's electric motors use rare-earth permanent magnets, specifically $Nd_2Fe_{14}B$. These magnets are used because their energy products, over 50 MGOe, are the best of any material. Figure 1.21 shows the development of permanent magnet materials and their current energy products.
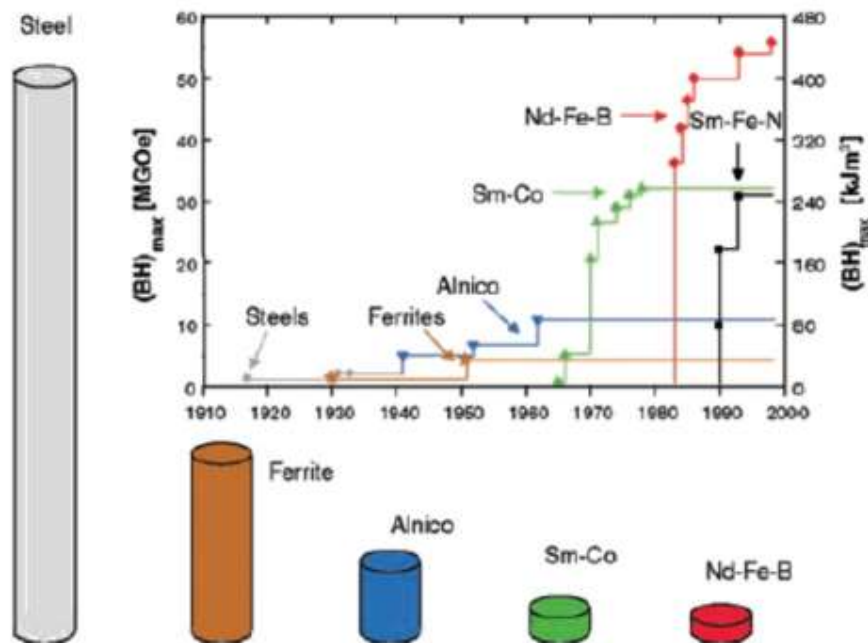
Figure 1.21: Permanent magnet energy products

Nd-Fe-B permanent magnets have the highest energy products available, making them the ideal choice for electric vehicle applications. From [1].

Rare-earth permanent magnet's high energy product is a result of coupling of the rare-earth's high anisotropy layers and transition metal layers with high magnetic moments [6]. Figure 1.22 shows the crystal structure of $Nd_{12}Fe_{14}B$; note the alternating layers of rare-earth and transition

metal atoms. This allows for a high coercivity due to the high anisotropy resulting from the layered structure. At the same time the large amount of transition metal atoms contributes to a high saturation magnetization.
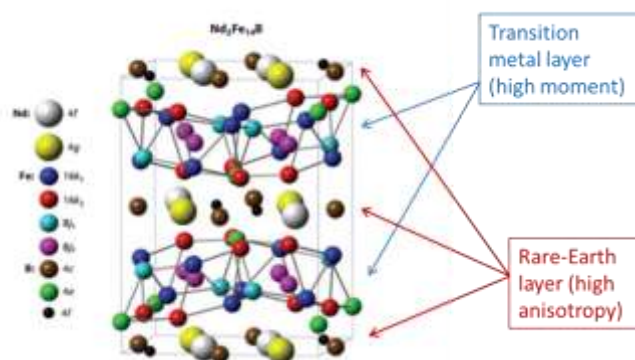
Figure 1.22: Nd$_2$Fe$_{14}$B crystal structure

The high energy product in Neodymium magnets is a result of the coupling between the high anisotropy layers and the high moment transition metal layers. From [6].

There are two major issues with using Nd-Fe-B permanent magnet motors in traction drive and turbine applications. The first is the amount of material required for these applications. Previous applications such as speakers, CD/DVD, and mobile phones require small amounts of the magnetic material. In traction drive applications the weight required is in the kilograms per vehicle, and even higher in wind turbine applications. The second is that Nd-Fe-B magnets do not perform as well at elevated temperatures. To counteract this loss of performance at higher temperatures, Dy is substituted for Nd in quantities as high as 12 wt% [6]. The addition of Dy slightly improves the Curie temperature and dramatically increases the coercivity due to increased anisotropy constants. As operating temperature increases, the loss in coercivity in the Dy containing magnet from temperature effects has a smaller impact on energy product. The

addition of Dy lowers the room temperature value for energy product because of the reduction in

magnetization due to the fact that the Dy atoms couple in an antiparallel direction with the Fe

atoms [7]. However, Dy is a critical material that is susceptible to price fluctuations. Figure 1.23

shows the effect that the addition of Dy has on coercivity and B_r.
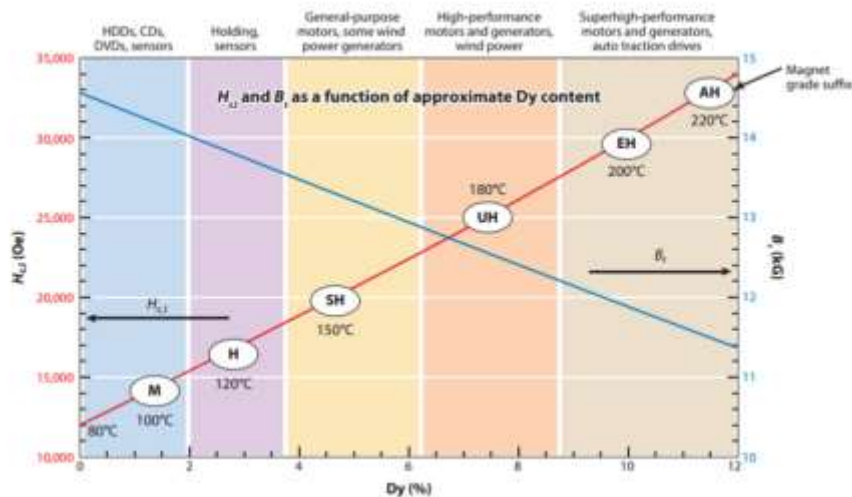
Figure 1.23: Impact of Dy addition in Nd-Fe-B

As Dy content increases so does the coercivity, while the remanent magnetization is

reduced. From [6].

Because of these supply chain instabilities and the large quantity required for vehicles, some

electric vehicle companies, such as Telsa Motors, have decided to use the less efficient induction

motors [8]. Sm-Co is another type of rare-earth permanent magnet with better high temperature

performance; however, the energy product of this material is less than that of Nd-Fe-B and is

subject to similar rare-earth supply issues. The goal of this thesis is to find a replacement

material that can be relied upon even as larger quantities are required and electric vehicles and

renewable energy sources become more common place. The next sections will discuss possible replacement materials for these Nd-Fe-B magnets.

ii. Alnico

There are two types of rare-earth free permanent magnets in production, Alnico and ferrites. Alnico magnets hold the current record for highest rare-earth free energy product in production. These materials are produced with energy products as high as 10 MGOe [1]. Alnico is a unique type of permanent magnet material because it has very low magnetocrystalline anisotropy. Instead of relying on magnetocrystalline anisotropy, alnico magnets rely on shape anisotropy. Shape anisotropy refers to anisotropy that derives from the grain shape and orientation rather than the crystal structure. In alnico, FeCo rods are formed in a NiAl-rich matrix via spinodal decomposition. Even though the FeCo has a cubic structure with no uniaxial anisotropy, if the aspect ratio of the rods is large (5-10) which develops shape anisotropy with the easy axis occurring along the length of the rod [4], (figure 1.24).
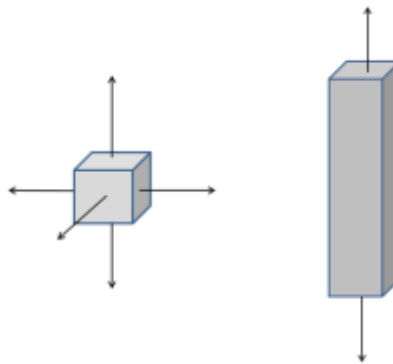
Figure 1.24: Shape Anisotropy

Shape anisotropy can reduce the number of easy axes by creating a preferred direction along the length of the rod.

In alnico these rods are developed by spinodal decomposition from a high temperature phase into the separate FeCo and AlNi phases. Current alnico magnets are formed by annealing under the influence of a magnetic field that causes the FeCo rods to from in a single direction creating an anisotropic bulk magnet. The advantages of alnico include a high M_s and high T_c, which make it a strong candidate for high temperature applications like traction drive due to the low temperature dependence of the magnetic properties (figure 1.25). The drawback to alnico is its low coercivity due to its dependence on shape anisotropy. Alnico's energy product could continue to be improved as the coercivity of the material is improved.
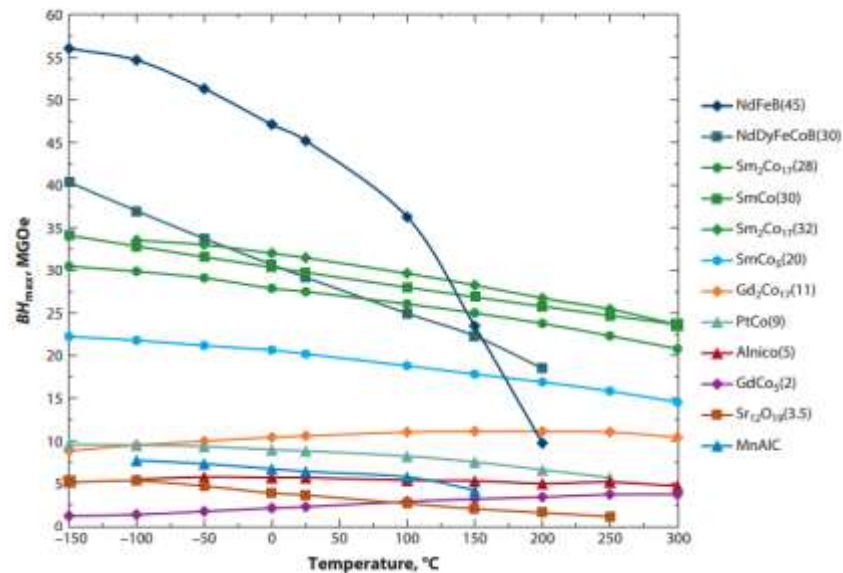
Figure 1.25: Temperature dependence of BH$_{max}$ of various materials

Alnico has much more stable properties as temperature increases than the Nd-Fe-B magnets alloyed with Dy.

iii. Future Rare-Earth Free Magnets

There are a variety of rare-Earth free permanent magnet materials that are currently being research and are not yet in production. This section will discuss the most likely candidates to surpass alnico. Table 1.1 is a table of permanent magnet materials, listing their anisotropy constant along with saturation magnetization.

material	K (ergs/cc $*10^7$)	Ms emu/cc
FePd	1.8	1100
FePt	6.6	1140
CoPt	4.9	800
MnAl	1.7	560
MnGa	1.2	250
$HfCo_7$	1.0	870
YCo_5	5.5	840
MnBi	0.91	610
Mn_2Ga	2.35	45
FeNi	0.5	1125
Fe_3O_4	0.011	480
$SmCo_5$	17.2	860
Sm_2Co_{17}	4.2	970
$Fe_{14}Nd_2B$	4.6	1270

FePd, FePt, CoPt → High cost

$SmCo_5$, Sm_2Co_{17}, $Fe_{14}Nd_2B$ → Rare earth material

Table 1.1: Anisotropy constant and magnetization values

Blue: rare-Earth materials, Red: materials with costs above that of rare-Earth,

Compiled from the references found starting on page 96.

a. Fe-based

Most Fe-based permanent magnets are already in production. Alnico has already been discussed in length. Ferrite is another material currently in production and composes the largest portion of the permanent magnet market, by weight [6]. Ferrite energy products are limited by the materials' low magnetizations, caused by the ferromagnetic structure spin structure (figure 1.5). The Fe atoms align in a parallel or antiparallel direction based on their position within the

ferrite crystal structure. FeNi is a material that is currently being researched that has the possibility to be a solution to the search for a rare-earth free permanent magnet with a high energy product. FeNi in the $L1_0$ structure has magnetization values similar to that of Nd-Fe-B as well as a relatively high anisotropy constant. Tetrataenite FeNi has an $L1_0$ structure similar to that of FePt and FePd materials used in magnetic recording. This layered $L1_0$ structure creates uniaxial anisotropy resulting in good anisotropy constants that allows the material to be used in permanent magnet applications.
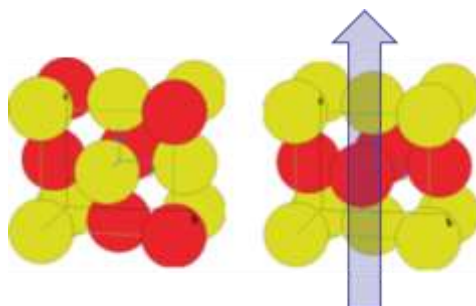
Figure 1.26: Disordered FCC and ordered $L1_0$

The layered structure in $L1_0$ allows for magnetocrystalline anisotropy that is not present in the disordered FCC structure.

Tetrataenite has the advantage of being composed of two low cost and readily available elements in Fe and Ni; however it poses other issues. Often times the $L1_0$ structure is not found on Fe-Ni phase diagrams and is most commonly seen in meteorites. This is because the ordering transition from the disordered FCC to the ordered structure occurs at a slow rate, on the order of millions of years. This long, slow cooling process that occurs as meteorites travel through space is difficult to replicate in the laboratory. Current research focuses on creation of this phase on a laboratory scale, as bulk magnets have yet to be produced. Most efforts focus on the creation of

atomic vacancies increase atomic diffusion rates to allow for the ordering to occur on a more

reasonable time scale, as well as the creation of thin film and nanoparticles in order to better

study the structure [9] [10] [6].

b. Mn-based

Mn-based materials have also received consideration as permanent magnetic materials.

Recalling the Bethe-Slater curve (figure 1.3) Mn naturally occurs as antiferromagnetic due to the

interatomic spacing being too small for ferromagnetic coupling to occur. However the magnetic

moment of a transition metal atom is heavily dependent on the number of unbalanced electron

spins in the d-shell. Mn has all five electrons in an unbalanced state, more than both Fe and Co

(figure 1.27). Mn-based permanent magnets try to take advantage of this high moment. Mn-

based magnets achieve this by using alloying elements to increase the exchange distance

between Mn atoms in the lattice to induce ferromagnetic coupling.

	+2	+1	0	−1	−2	S	L	J
$3d^1$ Ti^{3+}, V^{4+}	↓	—	—	—	—	1/2	2	3/2
$3d^2$ V^{3+}, Cr^{4+}	↓	↓	—	—	—	1	3	2
$3d^3$ Cr^{3+}, Mn^{4+}	↓	↓	↓	—	—	3/2	3	3/2
$3d^4$ Cr^{2+}, Mn^{3+}	↓	↓	↓	↓	—	2	2	0
$3d^5$ Mn^{2+}, Fe^{3+}	↓	↓	↓	↓	↓	5/2	0	5/2
$3d^6$ Fe^{2+}, Co^{3+}	↑↓	↑	↑	↑	↑	2	2	4
$3d^7$ Co^{2+}, Ni^{3+}	↑↓	↑↓	↑	↑	↑	3/2	3	9/2
$3d^8$ Ni^{2+}, Co^+	↑↓	↑↓	↑↓	↑	↑	1	3	4
$3d^9$ Cu^{2+}, Ni^+	↑↓	↑↓	↑↓	↑↓	↑	1/2	2	5/2

Figure 1.27: Spin structure of transition metal ions [4]

MnBi has been studied as a viable permanent magnet material. MnBi has the potential to form a

NiAs structure shown in figure 1.28.
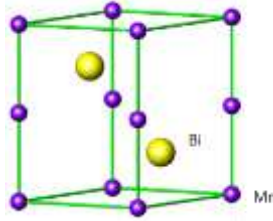
Figure 1.28: MnBi crystal structure

From [12]

This high anisotropy phase is referred to as the LTP, low temperature phase (K= $0.91 \cdot 10^7$ ergs/ cm^3, M$_s$= 610 emu/cm^3). Creating MnBi samples with only the LTP phase has proven to be a difficult challenge. Mn atoms tend to separate and form a separate phase. Through rapid solidification samples as high as 95% pure LTP have been synthesized [11]. The MnBi alloy is unique from others in that the coercivity increases with temperature, something not found in any other material.
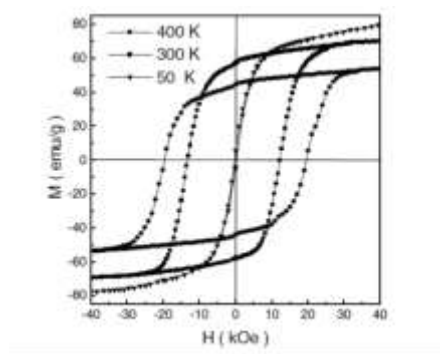
Figure 1.29: Hysteresis dependence on temperature in MnBi

MnBi shows unique magnetic behavior in that the coercivity increases with increasing

temperature. From [12]

While that exact reason for this increasing coercivity is unknown, it has been suggested that it is related to the spin-orbit coupling of the atoms [13]. This increasing coercivity makes MnBi a strong candidate for traction drive applications where the operating temperature will be high. However the magnetization of MnBi drops sharply with temperature, meaning the coercivity and magnetization are never maximized at the same temperature. Plots of coercivity and magnetization as functions of temperature can be seen in figure 1.30.
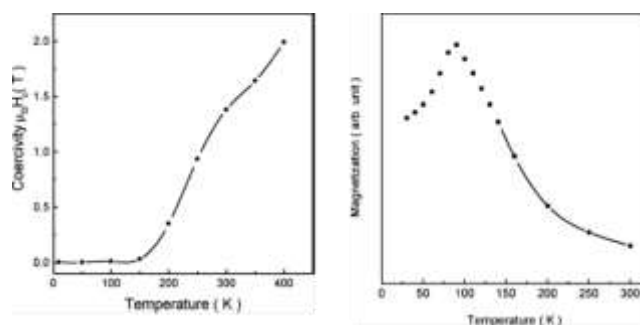
Figure 1.30: Coercivity and magnetization dependence of MnBi

While the coercivity of MnBi rises with temperature, the magnetization drops sharply after 100K. From [11].

Another Mn-based material studied is Mn_xGa. Mn_xGa has a broad range of compositions. MnGa has an $L1_0$ structure however the more commonly studied compositions have increased Mn concentrations up to Mn_3Ga. For values $1<x<2$, the material is considered $L1_0$. Above this composition in the range $2<x<3$, the crystal structure is considered $D0_{22}$ (figure 1.31). This $D0_{22}$ structure results in a higher magnetocrystalline anisotropy that leads to a higher coercivity, but at the cost of a reduced magnetization due to the antiferromagnetic coupling between the excess Mn atoms.
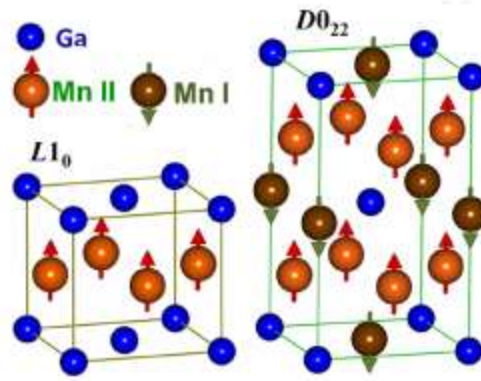
Figure 1.31: Mn$_3$Ga D0$_{22}$ structure

In the D0$_{22}$ structure, excess Mn atoms are located in the Ga layer of the structure and couple antiparallel to the Mn layers, causing the creation of a ferrimagnet with low magnetization but high uniaxial anisotropy. From [14].

In the Mn-Ga system the highest experimental energy product of 3.4 MGOe occurs at the 1:1 stoichiometry with the L1$_0$ structure [14]. One of the major driving factors in the thesis of the D0$_{22}$ structure in addition to the increased coercivity is the cost of Ga. Ga is an expensive material, almost on the scale of the rare-Earths on a per kilogram basis, which makes the L1$_0$ MnGa a poor candidate for traction drive applications. However it is still a commonly researched material in thin films for magnetic recording [10, 15,16].

The final Mn-based material that will be discussed is another L1$_0$ type alloy, MnAl. This material consists of alternating layers of Mn and Al resulting in uniaxial anisotropy similar to that of the other L1$_0$ alloys. The advantages of MnAl include a low raw materials cost, high anisotropy constants, and scalable production to bulk material. Previous research has demonstrated successful formation of the precursor high temperature ε phase by quenching of the ingot [53,55] and by rapid solidification [40]. This ε phase can then be annealed at

temperatures between 400°C and 500°C to form the $L1_0$ phase [39,40,52,53,54,55]. In both FeNi and MnGa, bulk magnets have yet to be produced in the laboratory, and attempts with MnBi have yet to yield a 100% phase pure magnet. MnAl does not have as high of a potential energy product as FeNi, due to FeNi's high magnetization, but is much closer to production ready for large scale applications. MnAl is not without its issues, mostly due to the $L1_0$ structure's metastable nature. Improvement of the Mn-Al energy product has focused on microstructural control via mechanical milling [39,52,55]. These studies have shown success in improvement of the materials coercivity, however these studies also show a decrease in magnetization during the milling process. The addition of small amounts of C have shown to help stabilize the $L1_0$ phase [39,54], however the addition of 2% C lowers the Curie temperature of the material from 346°C to 258°C[54]. This material would be discussed in more detail in Chapter 3.

c. Co-based

As mentioned in the rare-earth section, Sm-Co magnets are another type of rare-earth permanent magnets in production. $SmCo_5$ is one of the alloys currently in production as a permanent magnet. This has led researchers to try to create similar structures with the larger atoms in groups 3 and 4, specifically Zr and Hf. These materials have been synthesized as bulk materials with excellent materials properties (table 1.1). While synthesis of these materials is far ahead of some of the other materials discussed, such as FeNi, MnGa, and MnBi, they may be the least understood materials from a crystallographic point of view. Numerous researchers have indexed their crystal structure to orthorhombic, tetragonal, or rhombohedral structures [18-27]. Advantages of these materials include uniaxial anisotropy and high magnetizations, along with easily scalable production methods. However the drawback is the lack of knowledge about the

crystal structure that makes it difficult to predict the energy products that can be achieved in the future.

II.   Experimental Procedure

1. Sample Preparation

All alloys were prepared by arc-melting in Ar atmosphere (Ar gas: Matheson UHP). Following the arc-melting, samples were melt spun (0.8mm orifice, 0.5 bar back pressure) using a Cu wheel in an Ar atmosphere. Mechanical milling was performed using steel vials in a SPEX mixer/ mill 8000. The SPEX mill was setup to mill for one minute intervals on, than one minute off to reduce thermal fluctuations. Milling vials were sealed in a nitrogen atmosphere glove box. In surfactant milling oleic acid was used as the surfactant in a ratio of 1:2 surfactant to sample by weight. For heat treatments samples were sealed in a quartz tube with Ar gas and hat treated in a tube furnace.

2. X-ray Diffraction

This thesis will use x-ray diffraction as a method of investigating the crystal structure of the materials and phases present. X-ray diffraction involves the use of x-rays generated with a specific wavelength (all experiments in this thesis were done with Cu K-α radiation, wavelength $\lambda=1.5418$ Å) to describe the planar spacings within a lattice. The basis of x-ray diffraction experiments is Bragg's law. Bragg's law describes the relation between the x-ray's wavelength, the incident angle, and the planar spacing. Bragg's law is: $n\lambda=2d_{hkl}sin\theta$ [28]. When this Bragg

condition is met, constructive interference occurs and the reflected wave intensity is high. Figure

2.1 shows the experimental setup used to find the Bragg condition for a specific set of planes.
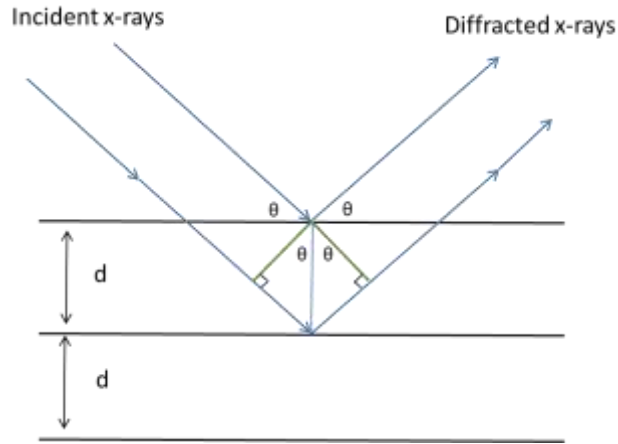
Figure 2.1: Bragg's law

X-ray diffraction involves scanning a range of angles and measuring the intensity of the reflected

wave. Once the angle θ where constructive interference occurs is identified, and the planar

spacing d calculated from Bragg's law, the peak can be linked to the corresponding *hkl* values.

For a given crystal structure the planar spacing "d" is a function of *hkl* and the lattice parameters.

For example, in the cubic system: $\dfrac{1}{d^2} = \dfrac{h^2+k^2+l^2}{a^2}$. By comparing the "d" spacing to the

hkl values of a given structure it can be determined if the material's atoms are arranged in the

given lattice. The allowed reflections for a given lattice can be found by the structure scattering

equations [30]. The amplitude of a wave scattered by a single unit cell is defined by the equation:

$F_{hkl} = \sum_{i=1}^{n} f_i \cdot e^{2\pi i(hu+kv+lw)}$ where f_i is the scattering factor for the atom and (h,k,l)

correspond to lattice directions. The scattering factor for atoms is related to the atomic number. It

is therefore possible for samples with multiple elements to have diffraction planes that are not

seen in a single element sample, these peaks are known as superlattice peaks. In this thesis two

diffractometers were used, a Rigaku Multiflex and a PANalytical Empyrean.

3. Magnetic Measurements

The measurement of the magnetic hysteresis loop was discussed at length in chapter 1.

The hysteresis loops in this thesis were measured using a Lakeshore 8500 VSM and Quantum

Design SQUID. A unique method was used in the sample preparation for magnetic measurement

samples in an attempt the measure accurately the magnetization of the powder as well as test for

the existence of single crystal particles (figure 2.2). The powder's mass was measured and then

placed in a capsule. A magnetic field was then applied to the powders using a Nd-Fe-B magnet.

Epoxy was added to hold the particles in place and cured while still under the influence of the

permanent magnet's field. If single crystal particles exist within the sample, this process will

cause the appearance of texture when the magnetic properties of the sample are measured due to

the alignment of the c-axes of the particles with the magnetic field generated by the Nd-Fe-B

magnet.
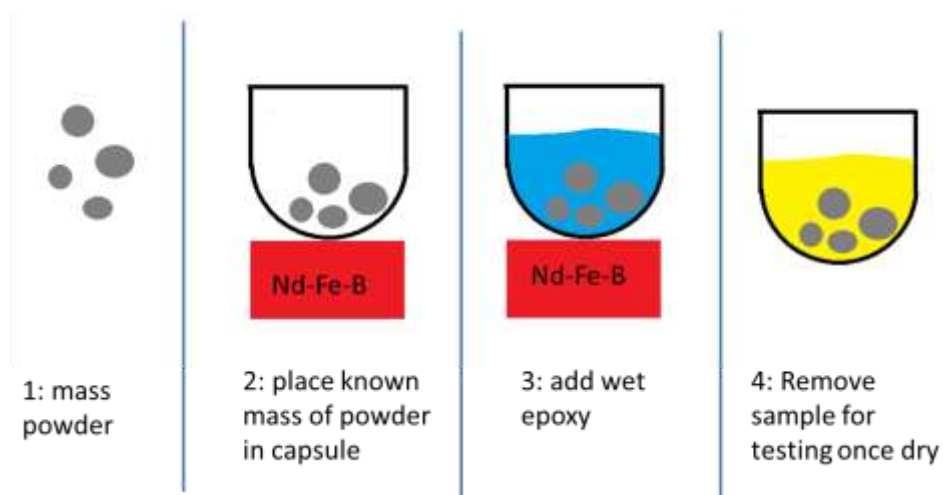
Figure 2.2: Procedure for creating magnetic measurement samples

All samples were pulse magnetized with a field of 10 T before the hysteresis loops were measured in order to make sure the material was completely magnetized in the starting direction.

4. Electron Microscopy

All imaging done in this thesis used electron microscopy. Both scanning electron microscopy (SEM) and transmission electron microscopy (TEM) were used. Both of these techniques generate electrons and concentrate them through a series of magnetic lenses. In the SEM the secondary electrons are generated by the interaction of the electron beam with the sample by ejecting the valence electrons from near the sample surface [31]. This allows the SEM to image surface features, however it does not contain atomic number or elemental information when imaging using the secondary electrons. The image in the SEM is created by collecting the electrons one point at a time, similar to pixels in a digital image, by scanning the electron beam across the surface. The experimental setup for the SEM is shown in figure 2.3.
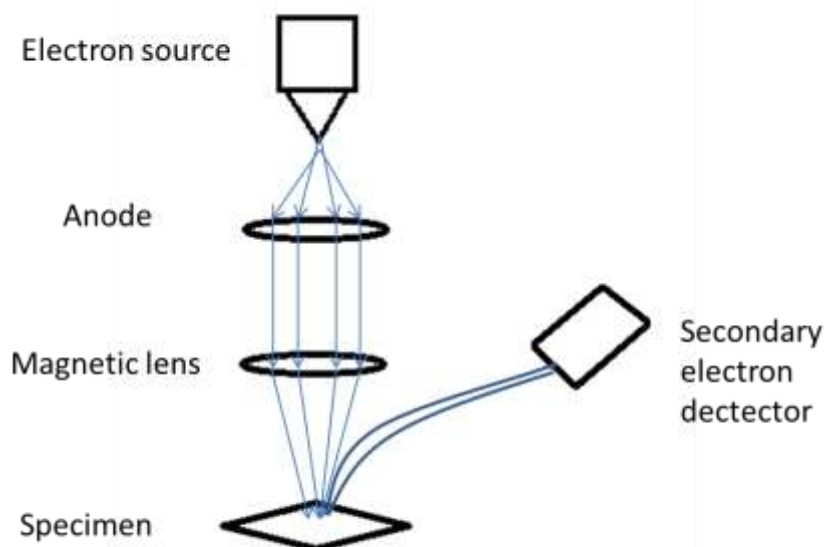
Figure 2.3: SEM microscopes

SEM is primarily useful in the milling studies. It allows the study of the morphology of the

particles, the particle size, and can image the fracture surfaces. All imaging in this thesis was

performed with a FEI NanoSEM operating at 15kV and a working distance of 5mm.

The second type of electron microscopy is transmission electron microscopy. Unlike the

SEM, the TEM does not collect the secondary electrons but instead passes an electron beam

completely through the material and collects the electrons on the other side (figure 2.4). Also

unlike the SEM, the entire area is imaged simultaneously in the TEM. As the electrons pass

through the sample they are scattered and pass through lenses below the sample. From here they

are redirected where they are collected and the image is magnified. TEM is used in this thesis for

imaging of grains and grain boundaries. Limitations of the TEM include the sample thickness,

which must be less than 100Å, as well as the projection of a 3 dimensional sample as a 2

dimensional image.
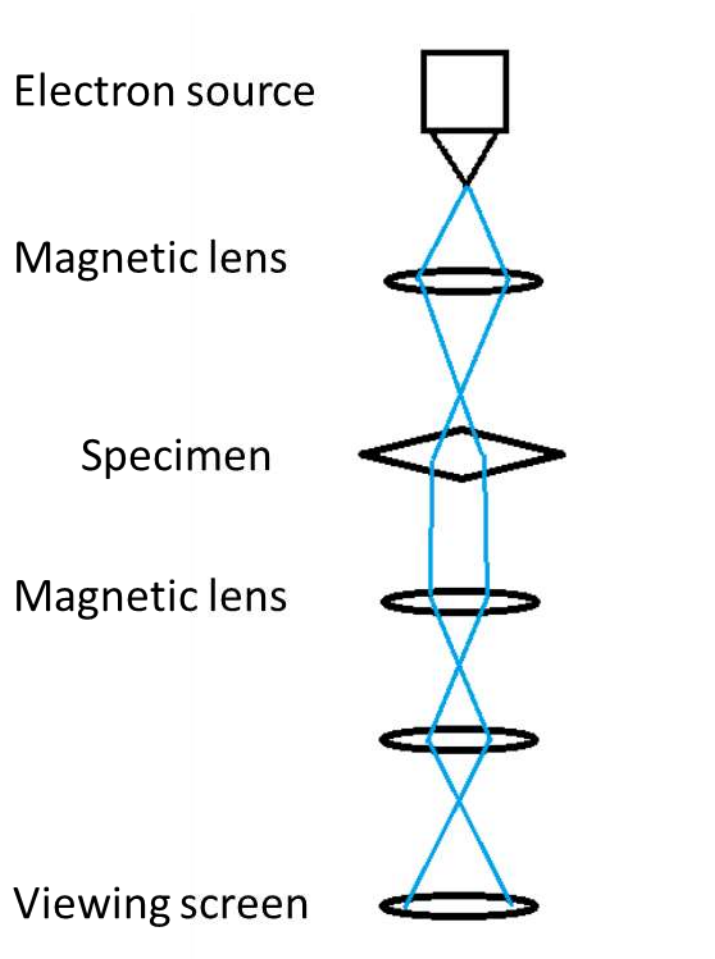
Figure 2.4: The TEM

All TEM images for this thesis were taken using an FEI Osris 2014 operating at 200kV.

III. Mn-Al

1. Background

Chapter one discussed the permanent magnet alloy Mn-Al. This alloy was studied to attempt to improve both its intrinsic and extrinsic properties followed by hot pressing into fully dense bulk magnets. The $L1_0$ phase, also referred to as the τ phase in the Mn-Al system, has relatively good intrinsic magnetic properties (K_1= 1.7 MJ/m^3, M_s=7.5 kG [34]), suggesting a

potential maximum energy product of ~12 MGOe with appropriate microstructural development

[35]. The L1$_0$ phase is metastable and forms from the high temperature ε phase, which is stable

above 870°C. The equilibrium phases at room temperature that normally result from the

decomposition of the ε phase are γ$_2$ and β-Mn [36]. The phase diagram is shown in figure 3.1.
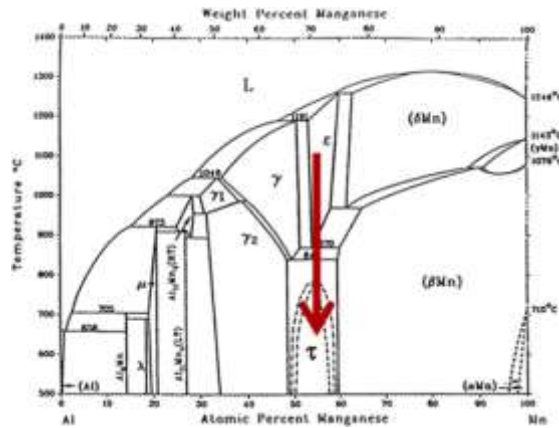
Figure 3.1: Mn-Al phase diagram

The L1$_0$ τ phase is formed by first forming the high temperature ε phase followed by

annealing. γ$_2$ and β-Mn are the stable phases that otherwise occur at this composition range

[36].

The high temperature ε phase is a disordered HCP structure. Through the melt spinning process,

this structure can be stabilized at room temperature where the high cooling rate suppresses

equilibrium phase formation. When the material is annealed at 500°C for a minimum of ten

minutes, a transition to the L1$_0$ ordered phase occurs. The composition of the L1$_0$ phase is

therefore controlled by the composition that can be achieved in the high temperature ε phase.

The reported values for the range of the ε phase are $0.40 < x_{Al} < 0.46$ [37]. This varies from the

ideal L1$_0$ composition. This results in an excess of Mn atoms in the L1$_0$ structure. These excess

Mn atoms occupy lattice positions in the Al-layers, and couple antiferromagnetically with the

Mn atoms in the Mn-layers and reduce the magnetization of the material (figure 3.2) [38].
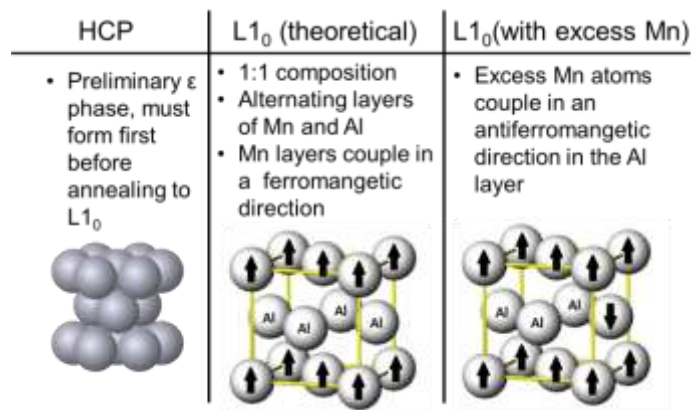
Figure 3.2: Mn-Al crystals

The composition of the L1$_0$ phase is controlled by the composition of the HCP ε phase.

These excess Mn atoms couple in an antiparallel direction.

This transition from the ε to τ phase is confirmed experimentally by XRD. Figure 3.3 shows

XRD patterns taken of melt spun sample before and after annealing.
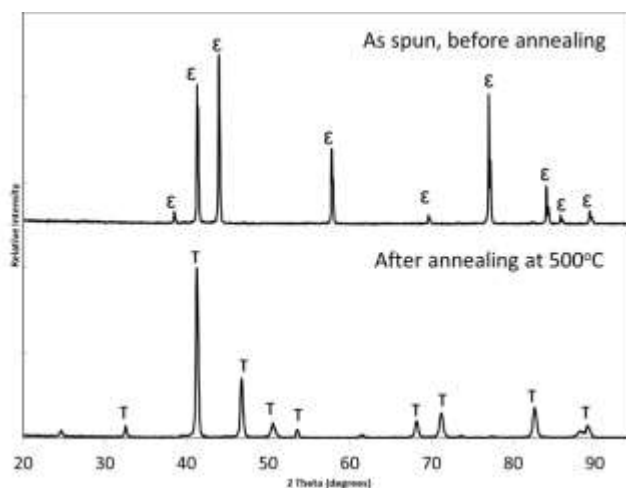
Figure 3.3: XRD of ε and τ

The addition of carbon to the $L1_0$ has been shown to help stabilize the $L1_0$ structure [AT, AU]. As well the addition of carbon affects one of the intrinsic properties, the Curie temperature, which is decreased from 392°C to 331°C with 1.7 atomic percent C. Up to 3% C helps to stabilize the $L1_0$ by interstitial substitution [39]. Outside of affecting Curie temperature, the carbon addition does not negatively impact any other magnetic properties.

2. Physical Metallurgy

The first step in optimizing the Mn-Al alloy was to identify the optimal chemistry for maximizing the energy product. The previous section showed that $Mn_{50}Al_{50}$ was not possible through rapid solidification because of the limits of the preliminary ϵ phase. Samples were created with the compositions of $Mn_{48.5}Al_{48.5}C_3$, $Mn_{51}Al_{46}C_3$, $Mn_{54}Al_{43}C_3$, and $Mn_{57}Al_{40}C_3$. After heat treatments of 500°C for 10 min the samples all formed combinations of the γ_2 , β , and τ phases (figure 3.4). The stoichiometric alloy $Mn_{48.5}Al_{48.5}C_3$ formed the γ_2 phase with no other identifiable phases. The $Mn_{51}Al_{46}C_3$ alloy was a mixture of the τ and γ_2 phases. The $Mn_{54}Al_{43}C_3$ alloy was the only one where pure τ phase material was achieved. The $Mn_{57}Al_{40}C_3$ alloy was a mixture of τ and β-Mn phases.
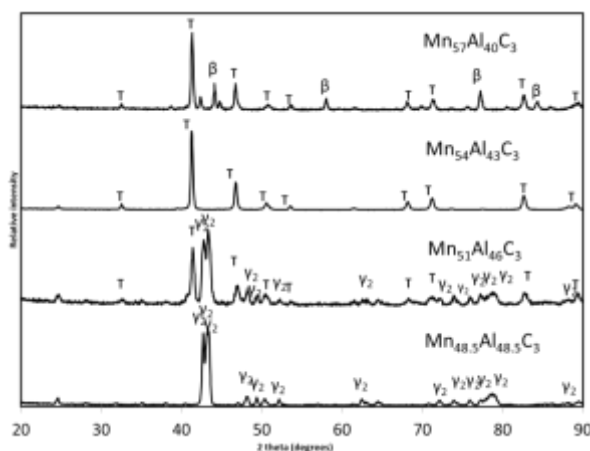
Figure 3.4: XRD for Mn-Al compositions

The $Mn_{54}Al_{43}C_3$ alloy was selected because it met the primary goal of a pure τ phase material, with the lowest possible excess Mn content. The previous section discussed the need for the alloy to be as close to the $Mn_{50}Al_{50}$ composition as possible due to the antiparallel orientation that lowers the saturation magnetization of the material, and therefore the energy product. Because of the existence of these antiparallel sites, the substitution of elements not normally used in magnetic alloys was investigated in addition to the more common choices of Fe and Co. The goal of the addition of elements such as Ti and Cu was to replace the antiparallel Mn atoms located in the Al layer with a lower moment to reduce the ferromagnetic effect, see figure 3.5.
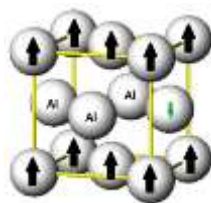
Figure 3.5: L1$_0$ structure

The goal with low moment materials is to reduce the anti-ferromagnetic moment from the excess transition metals in the Al layer and by result increase the saturation magnetization.

Alloys were created using the formula $Mn_{54-x}Al_{43}C_3T_x$ where "T" is the transition metal. The value of x was steadily increased for each transition metal until a second phase was formed. Figure 3.6 shows this process for the Fe samples. Samples were created until a B2 phase (figure 3.7) started to form at x=16, and as the concentration of Fe was further increased, the intensity of the B2 XRD peaks increased as well. The pattern was compared to similar B2 structures in the International Centre for Diffraction Data.
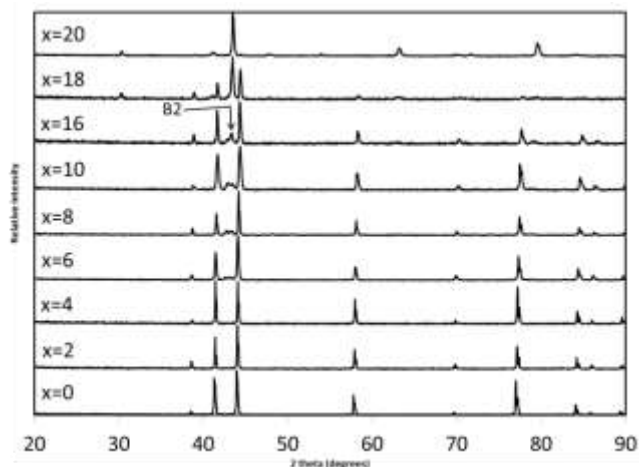
Figure 3.6: XRD for Fe as spun samples

x=16 is the first to show B2 formation, ratio of B2 to ε increases rapidly with further

addition of Fe.

The B2 structure is a cubic structure with low anisotropy. It is a layered structure with alternating

planes of the transition metals in a CsCl-type structure, see figure 3.7. However unlike the $L1_0$

structure, this does not result in a tetragonal structure and therefore does not result in uniaxial

anisotropy.
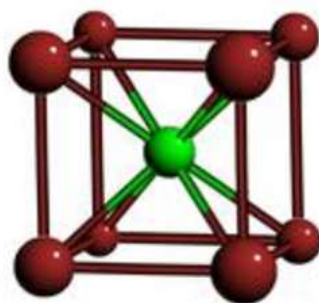
Figure 3.7: B2 structure

Similar experiments were done for Ni, Co, Ti, and Cu. Ni and Co immediately began to form the

B2 structure. Ti and Cu formed the ε phase up to x=6, resulting in a ratio where the number of

Mn atoms does not outnumber the available ferromagnetic lattice positions. XRD data from these series can be seen in figure 3.8.
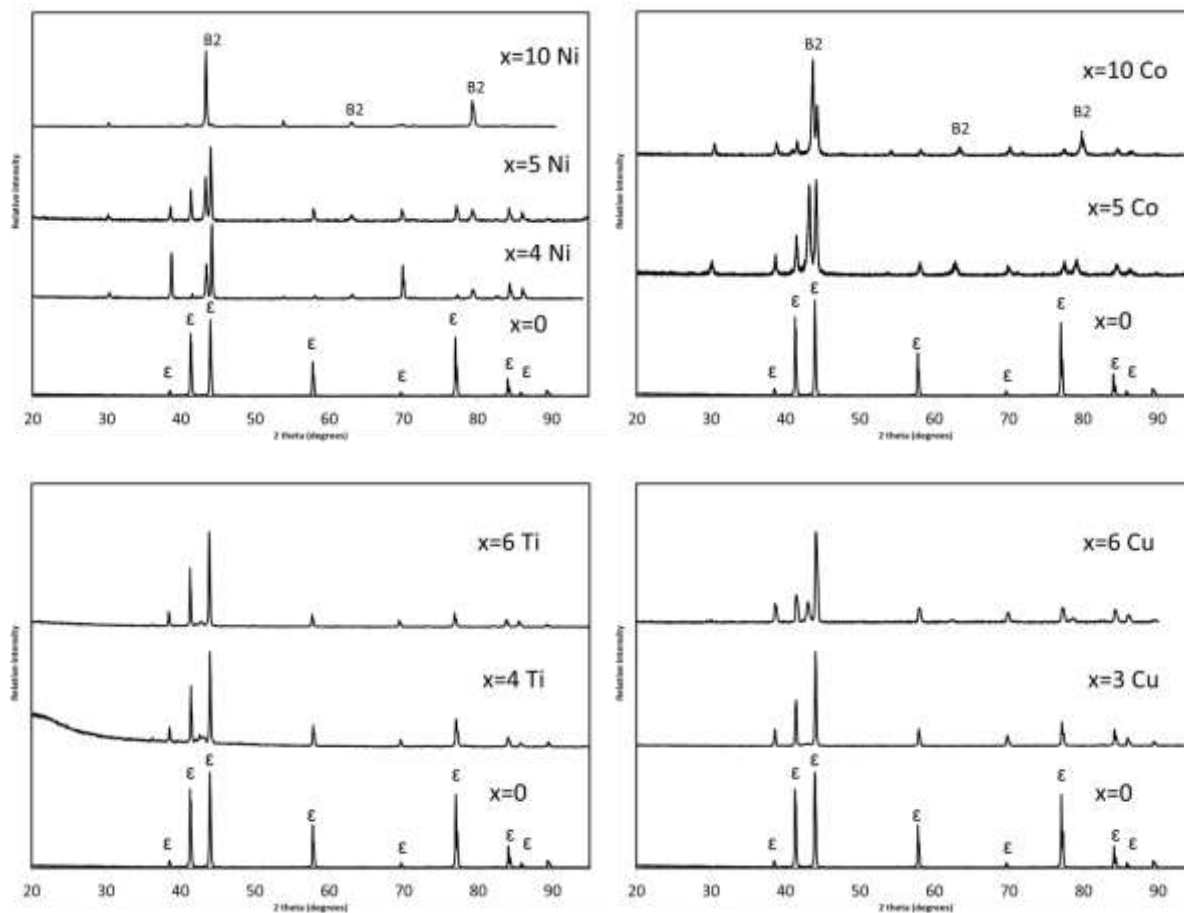
Figure 3.8: XRD of transition element additions

Ni and Co form a combination of ε phase and B2 in the as spun. Cu begins to form a secondary phase but due to the low intensity of the peak and lack of other peaks, this phase cannot be identified.

With the addition of Ti, the material was able to form the parent ε phase but when annealed at 500°C, the alloy transformed to the B2 phase instead of $L1_0$. Ti samples were then annealed at lower temperatures and for varying times in an attempt to determine conditions under which the $L1_0$ phase could be formed; however no conditions could be found (figure 3.9).
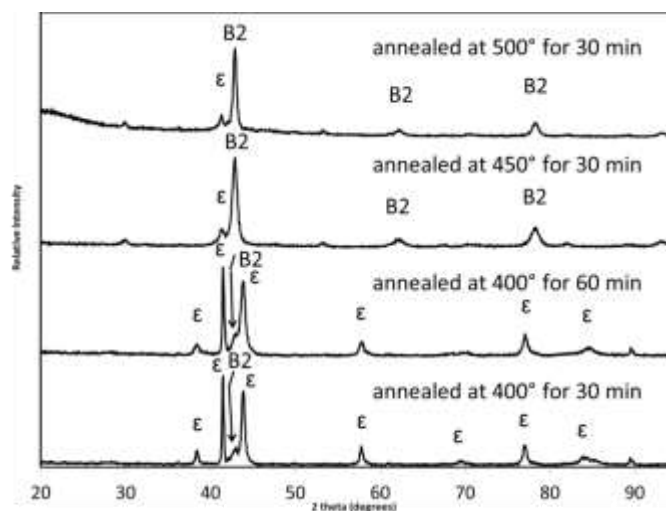
Figure 3.9: XRD patterns for annealed Ti samples

x= 6 Ti annealed at different times and temperature. As the annealing temperature

increases B2 begins to form before the temperature typical of the ε to τ transformation.

The alloys containing Fe and Cu formed the ε phase. Fe- containing alloys were then annealed at

500°C for 10 min to induce the phase change to $L1_0$. Up to x=6 the $L1_0$ phase was formed;

starting with x=8 the B2 phase was formed (figure 3.10).
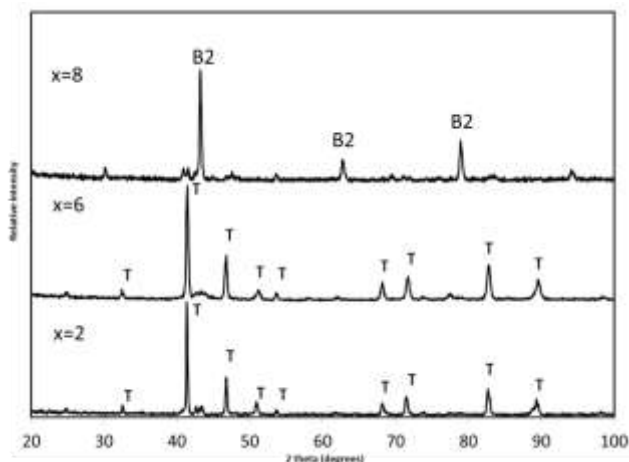
Figure 3.10: XRD for annealed Fe samples

x=6 forms $L1_0$ τ phase but beginning with x=8 B2 forms.

Similar to the Ti samples, lower temperatures and longer times were tested for the x=8 Fe

samples. Much like the Ti samples, the formation of the B2 structure in samples containing more

than x=6 Fe began before the formation of the L1$_0$. Therefore samples with x>6 were not

pursued as the B2 phase is not the phase of interest.

   Lower values of x were investigated for Cu addition (x=3 and x=6). Cu can improve the

results of densification during sintering [41], so its magnetic properties were investigated. The

XRD patterns from x= 3 Cu and x=6 Cu are shown in figure 3.11.
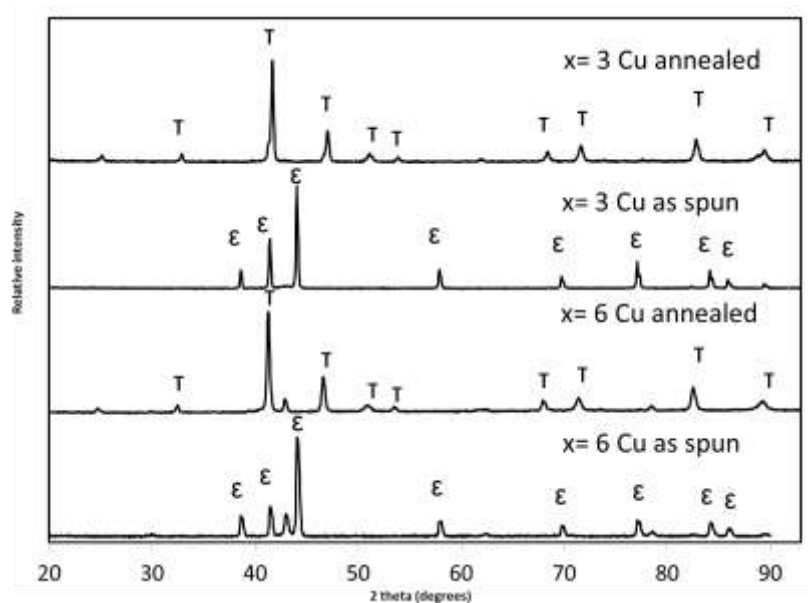
Figure 3.11: XRD for Cu samples

x=3 Cu and x=6 Cu both successfully form L1$_0$ phase. The peak of a secondary phase in the

6% Cu can be seen in both the as spun and annealed samples.

The non- indexed peak in the x=6 sample around 43° is mostly likely due to the β phase, but

since the amount of this phase is small this is the only peak present, and it is not possible to

index the peak conclusively.

Figure 3.12 is a flow chart for the selected transition metals. There were three possible outcomes when adding the transition metal atoms. The first was that the material immediately began forming the B2 structure; this occurred with the addition of Ni and Cu. The second possibility was that the transition metal was able to be dissolved into the ε phase, but when annealed the material transitioned to the B2 phase instead of the $L1_0$ structure, this occurred when Ti was added. The third possibility was that the element was successfully dissolved into both the ε phase and the τ phase, as was the case with Fe and Cu.

3 possibilities

Transition metal is insoluble in ε phase	Transition metal is soluble in ε phase but insoluble in $L1_0$ phase	Transition metal is soluble in both ε and $L1_0$ phases
Ni and Co	Ti	Fe and Cu
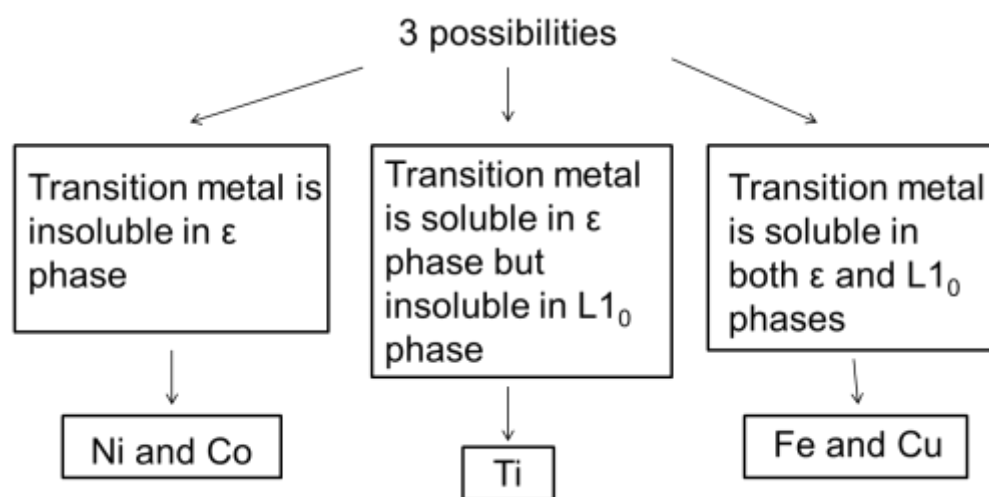
Figure 3.12: Transition addition flow chart

The magnetic properties of the $Mn_{48}Al_{43}C_3Fe_6$ and $Mn_{48}Al_{43}C_3Cu_6$ samples were compared to the x=0 sample. Both Fe and Cu additions lower the saturation of the material from 110 emu/g to 90 emu/g for the x=6 samples. For the T=Fe sample this is consistent with the first-principle supercell calculations found in reference [38] that show that Fe favors replacing the antiparallel Mn sites found in the Al layers of the $L1_0$ structure. Figure 3.13 shows the magnetic hysteresis loop of all three samples up to a field of 7 T.
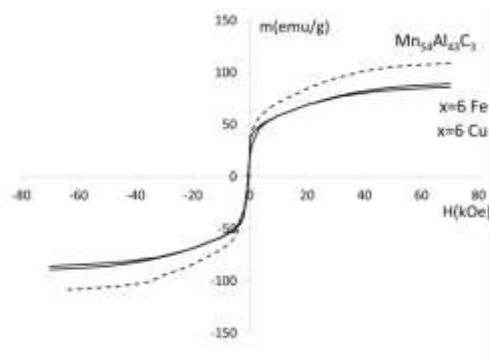
Figure 3.13: Hysteresis of x=6 samples.

The high field data shows a decrease in the saturation magnetization for both the Fe and

Cu substitutions.

The second quadrant shows that even though the T=Fe sample has a lower M_s, M_r remains the

same as the x=0 sample. As well, the coercivity for the T=Fe sample was unchanged compared

to the x=0 sample. Both samples containing Cu, x=6 Cu and x=3 Cu, samples had lower

coercivities, and the x= 6 Cu had a lower M_r than the x=0 sample (figure 3.14).
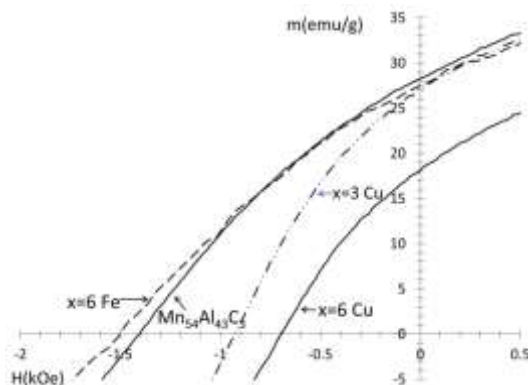
Figure 3.14: Second quadrant demagnetization curves for samples x=0, x=6 Fe, x=6 Cu, and x=3 Cu

The demagnetization curves for the x=0 sample and the x=6 Fe samples are very similar,

however the Cu samples show a decrease in coercivity, and in the case of the x=6 Cu a

decrease in the remanent magnetization.

Anisotropy constants were calculated using the relationship $M=M_0(1-A/H^2)+xH$. The constants were optimized using the sum of least squares for variables M_0, A, and x. These constants as well as the other magnetic data are summarized in table 3.1. These anisotropy constants are an intrinsic property, independent of the sample's microstructure, that relate to the maximum possible coercivity of the material.

composition	M_s (emu/g)	H_c (kOe)	K (ergs/cm^3)·10^7
$Mn_{54}Al_{43}C_3$	110	1.4	1.3
$Mn_{48}Al_{43}C_3Fe_6$	90	1.5	1.0
$Mn_{48}Al_{43}C_3Cu_6$	86	0.7	0.8

Table 3.1: Magnetic data for x=0, x=6 Fe, and x=6 Cu

This thesis confirms that the $Mn_{54}Al_{43}C_3$ composition is the best choice for permanent magnet properties. The addition of Fe does not increase magnetization or anisotropy constant, but does the opposite and decreases both of these values. The addition of Cu decreases magnetization, coercivity, and energy product, likely due to the formation of the second phase. However, its ability to ease consolidation could provide an increase in the overall energy product of the fully compacted magnet which will be demonstrated in section 4.

3. Mechanical Milling

With the $Mn_{54}Al_{43}C_3$ composition selected as the composition with the best properties for maximizing the energy product, mechanical milling was performed in order to create a favorable microstructure. Transmission electron microscopy showed an initial grain size of ~500 nm (Figure 3.15) in the as spun $Mn_{54}Al_{43}C_3$ alloy, while the corresponding selected area electron diffraction pattern (inset) indexed to the τ phase, with diffraction arising from multiple grains, consistent with the x-ray diffraction results. The high-energy mechanical milling thus was initiated on either single-phase ε (ε-milled samples) or single-phase τ (τ-milled samples). The ε-

milled samples were transformed to τ using the above-mentioned heat treatment, 500°C for 10

minutes. No post-milling heat treatment was done on the τ-milled samples, unless specifically

noted.
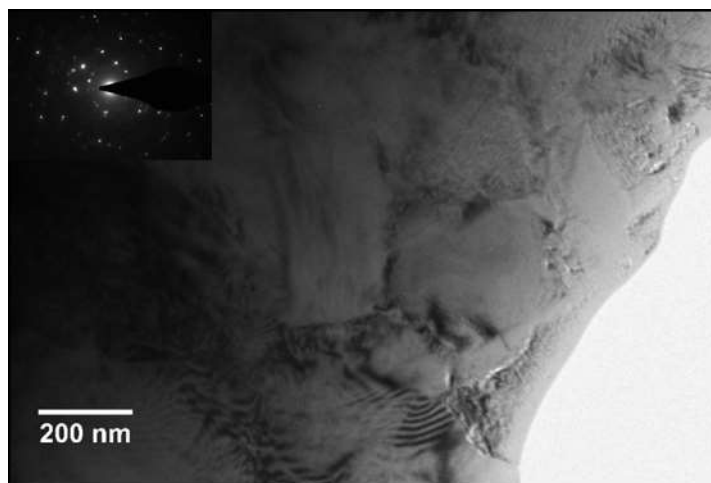
Figure 3.15: Transmission electron micrograph of melt spun Al-Mn-C after conversion to τ (inset: Selected area electron diffraction pattern of the region).

Mechanical milling of the initially τ phase samples resulted in a dramatic increase in the x-ray

diffraction peak widths (Figure 3.16). Additionally, the appearance of additional diffraction

maxima was observed between the two primary τ peaks (~45° 2θ). The major β-Mn peaks are in

this region, but the peaks are too diffuse to identify conclusively. After 3 h of milling, the τ

peaks are very broad, and further high-energy mechanical milling results in amorphization. For

the ε-milled samples, the peak widths of the τ phase (note that the sequence was milling in the ε

phase, followed by conversion to τ at 500°C for 10 min) were notably more narrow (Figure

3.17). The increased peak widths of the τ-milled samples were due to both grain size reduction

and increased structural disorder induced by the mechanical milling (notably, strain).

Conversely, the τ phase formed in the ε-milled samples would lack the structural disorder

induced by milling, similar to nearly defect-free grains that result from recrystallization, and the breadth of the diffraction peaks would solely be due to grain size effects. A secondary phase also evolves in the ε-milled samples, and in this case the peaks were positively identified to be from β-Mn.
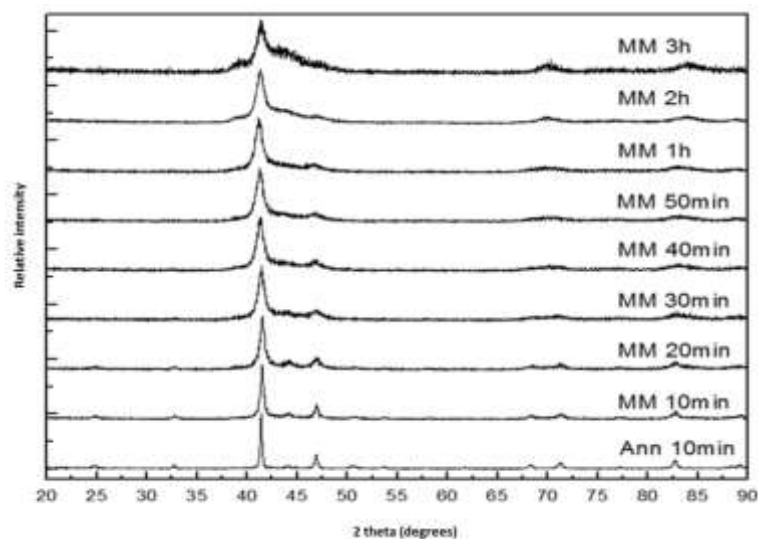
Figure 3.16: X-ray diffraction patterns for τ-milled samples for different milling (MM) times.

The bottom pattern is as-annealed (initial τ phase).
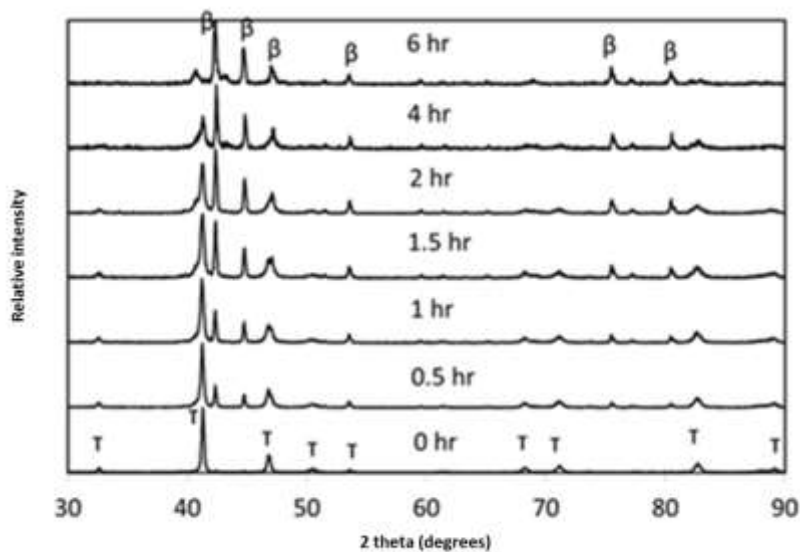
Figure 3.17: X-ray diffraction patterns for ε-milled samples after conversion from ε to τ.

In both ε-milling and τ-milling, the high-energy mechanical milling resulted in a significant

increase in the coercivity (Figure 3.18). Also in both cases, the initial increase in coercivity was

followed by a subsequent decrease upon further milling (Figure 3.19). The maximum coercivity

was similar in both cases (4.6 kOe for τ-phase milling, 4.1 kOe for ε-phase milling).

Additionally, the maximum was at similar milling times (1 h v. 1.5 h). However, the coercivity

of the ε-milled samples did not decrease as dramatically with further milling time. The coercivity

decrease in the τ-milled samples is likely due to amorphization or formation of the β-Mn phase,

where the amorphous phase is magnetically soft. However, because of the broad diffraction

peaks after milling it is not possible to distinguish between this amorphous material and the β-

Mn phase. In both cases, a dramatic loss of magnetization was also observed. The loss in

magnetization is much more significant in the τ-milled samples, but is also dramatic in the ε-

milled samples.
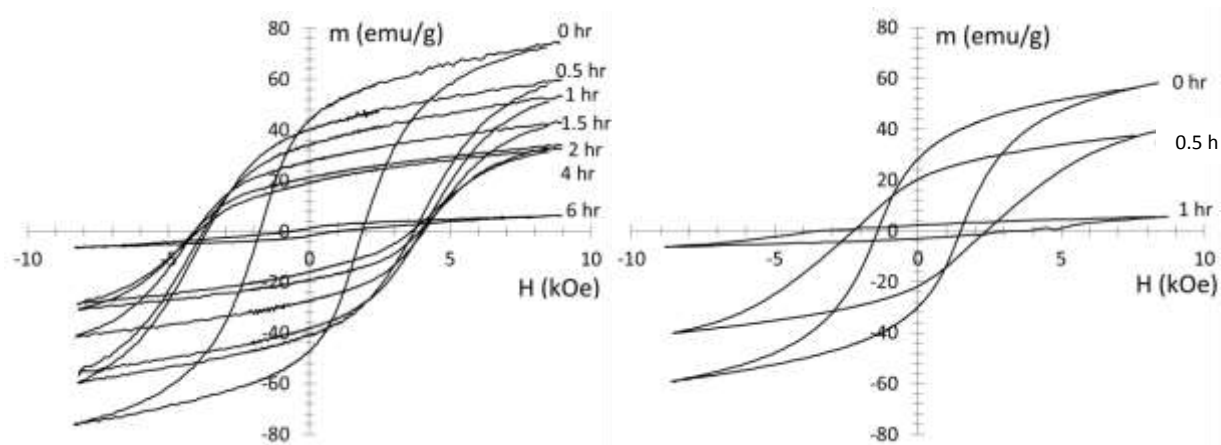
Figure 3.18: Hysteresis loops for milled samples

(a) Hysteresis loops for ε phase-milled samples for different milling times, after conversion

of ε to τ. (b) Hysteresis loops for samples milled in the τ phase.
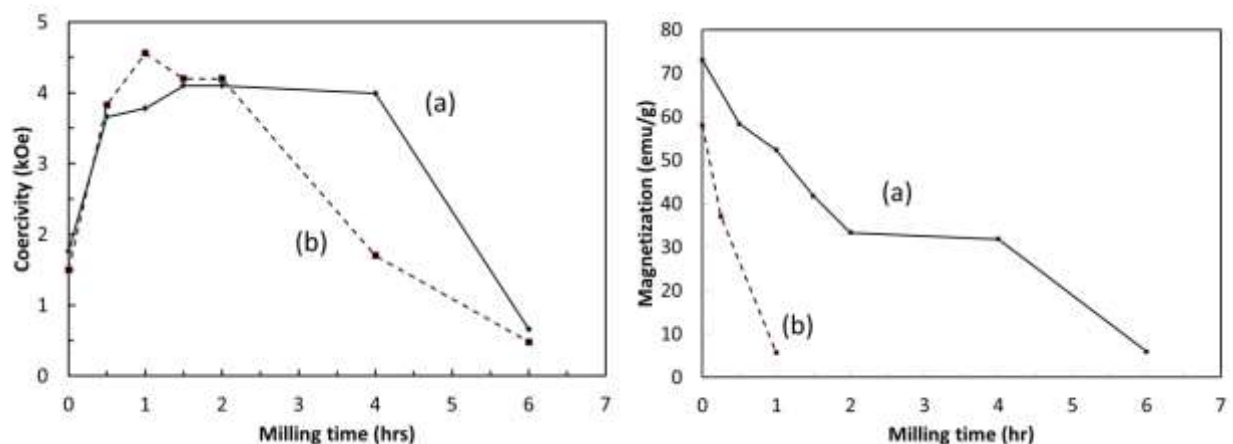
Figure 3.19: Relationship between coercivity, milling time, and magnetization (at 8 kOe) . Milling time for both the (a) ε milled (solid line), and (b) τ milled samples (dashed line).

The loss of magnetization with milling time may be attributed to the formation of the β-Mn phase, which reduced the phase fraction of the ferromagnetic τ phase. However, the loss in magnetization appeared more significant than the phase fraction of the β-Mn, particularly for the τ-milled sample. The loss of magnetization could possibly result from oxidation during milling, or from site disorder induced by the milling of the τ phase. The latter is essentially a loss of the long-range order, and the resulting antisite disorder resulting in antiferromagnetic coupling between Mn atoms along the c-direction.

If oxidation occurred during milling, then an effective change in Mn:Al ratio would result and the phase relationships would be altered. Thus, if a milled sample is annealed in the ε phase field (above 1050°C), then the phase transformation to the β phase can be reversed back to the ε phase, and ultimately form the τ phase. If oxidation occurred, the composition would shift so that it would no longer be in the ε single-phase field. Figure 3.20 shows a sample that was milled, annealed at 1050°C for 10 min, and then annealed at 500°C for 10 min. The XRD pattern

revealed single-phase τ, suggesting that no significant change in composition occurred that resulted in the formation of β-Mn during milling (Figure 3.17). Interestingly, the original coercivity was recovered upon conversion to τ, see figure 3.21 . Presumably, the grain size increased as a result of the high temperature heat treatment but returning the material to the original coercivity. Additionally, energy dispersive x-ray spectroscopy revealed only trace oxygen levels up to 1 h of milling, although long-term milled samples (10 h) showed significant oxidation. It should be noted that the mechanical milling protocol of the latter sample was different, notably that intermittent milling was not employed.
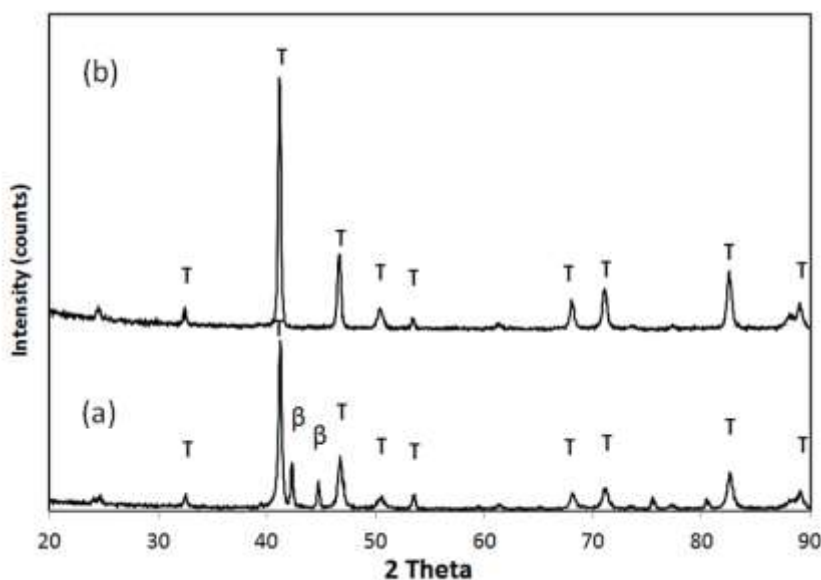
Figure 3.20: XRD for post annealed 1050°C samples

X-ray diffraction pattern (a) 1 h ε phasemilled sample, converted to τ showing significant phase fraction of β-Mn, and (b) same sample after annealing at 1050°C to transform the material back to ε, and then conversion to τ at 500°C for 10 min. It returns to single-phase τ.
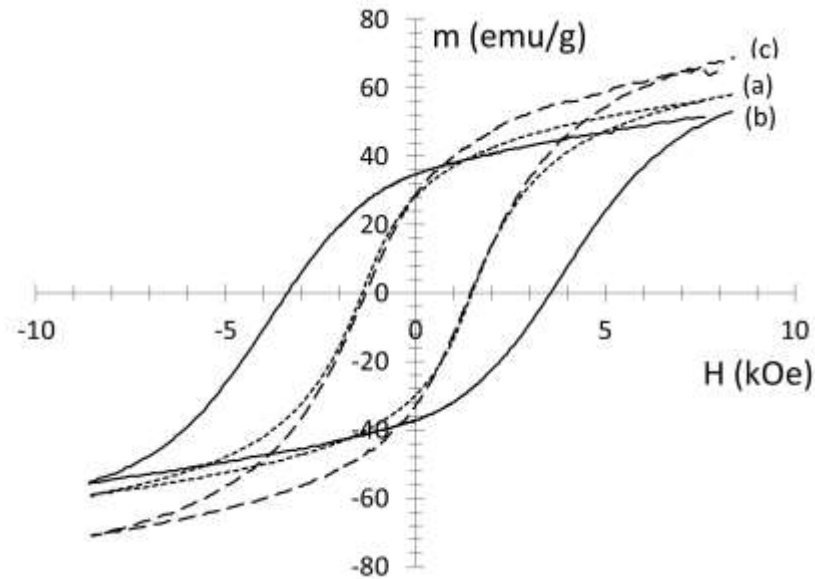
Figure 3.21: Hysteresis loops for post annealed 1050°C samples

(a) shows the initial hysteresis loop before annealing, (b) shows the material that has been milled for 1 hour in ε phase then converted to τ, and (c) same sample after annealing at 1050°C to transform the material back to ε, and then conversion to τ at 500°C for 10 min. After the conversion the magnetization is fully recovered, but the coercivity returns to the original value.

If the sample is annealed at a temperature below the ε field temperature (1050°C) then the grain size can still increase to the original size but the magnetization is not restored. Figure 3.22 shows the hysteresis loops for a sample that has been annealed at 850°C.
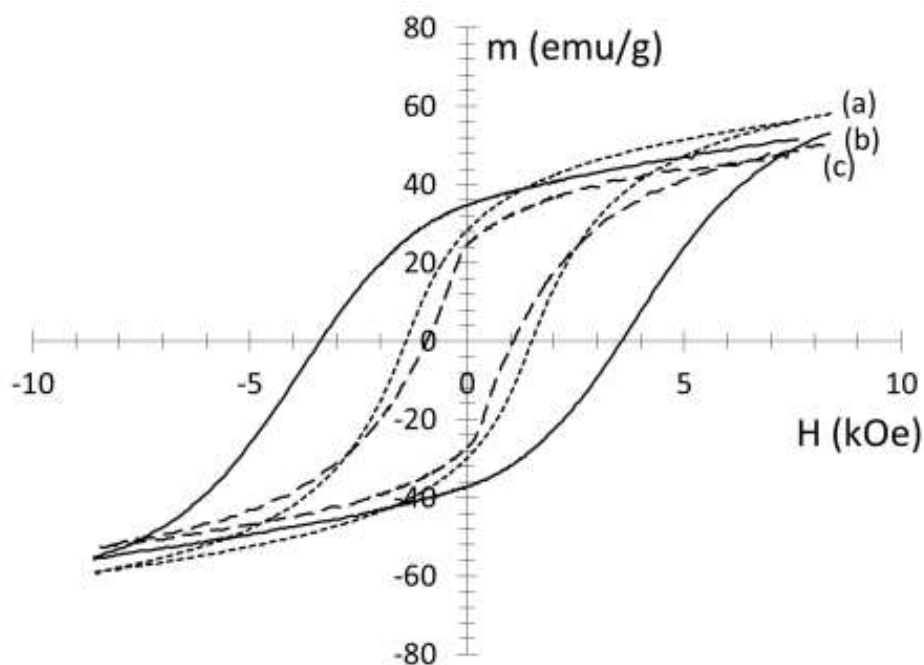
Figure 3.22: Hysteresis loops for post annealed 850°C samples

(a) Initial sample with no milling, (b) material that has been milled for 1 hour in ε phase then converted to τ, and (c) the same milled sample annealed at 850°C and then 500°C for 10 min. When the sample is only annealed at a temperature of 850°C the magnetization does not increase, and the material demonstrates noticeable two-phase behavior.

While these samples showed no oxidation effects on the magnetization, samples milled for longer time periods showed signs of oxidation in atom probe analysis. Figure 3.23 shows a 3-D atom probe reconstruction of the material before milling. The composition appears relatively homogenous throughout the sample and there are no signs of oxidation.

25 nm x 45 nm (thickness: 5 nm)
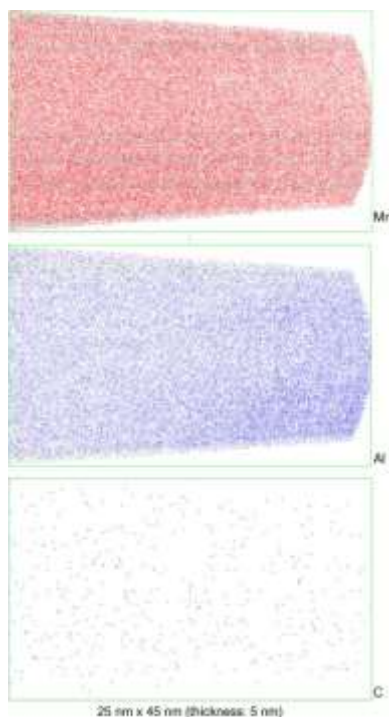
Figure 3.23: Atom probe for unmilled sample

Elemental distribution in a 5 nm thickness slice (perpendicular to the figure), in a

reconstructed volume (25 $\times$ 5 $\times$ 45 nm^3) of the unmilled sample.

In the milled sample, two types of regions can be observed: regions with no oxygen atoms that

contain Mn and Al, and regions with oxygen, containing Mn and Al in proportions that vary

throughout the investigated volume. C atoms appear to be homogeneously distributed in the

reconstructed volume. The mean measured compositions in this analyzed volume are $Mn_{60\pm5}Al_{40\pm5}$ and $Mn_{40\pm5}Al_{35\pm5}O_{25\pm5}$ for the so-called non-oxidized and oxidized regions, respectively. It is

worth noticing that the composition of the non-oxidized regions is close to Mn_3Al_2, which is the

compositional limit of the β-Mn phase. These results clearly show that the milled sample is

partly oxidized. Figure 3.24 reveals that at a nanometer scale, the microstructure is

heterogeneous. The size of the two regions can be estimated to be 10 - 30 nm. In figure 3.25 the

elemental composition profiles of Mn, Al and O elements at an interface between an oxidized

region and a non-oxidized region are shown (the corresponding region is displayed by the arrow

in figure 3.24).

45 nm x 113 nm (thickness: 5 nm)
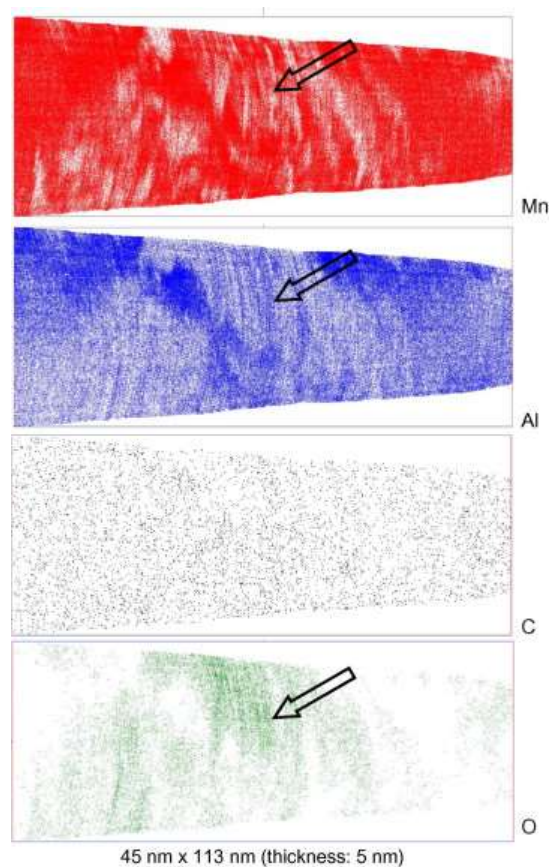
Figure 3.24: Atom probe for milled sample

Elemental distribution in a 5 nm thickness slice (perpendicular to the figure), in a

reconstructed volume ($45 \times 5 \times 113$ nm^3) of the milled sample. The arrow indicates the

area corresponding to the elemental composition profiles shown in figure 3.25.
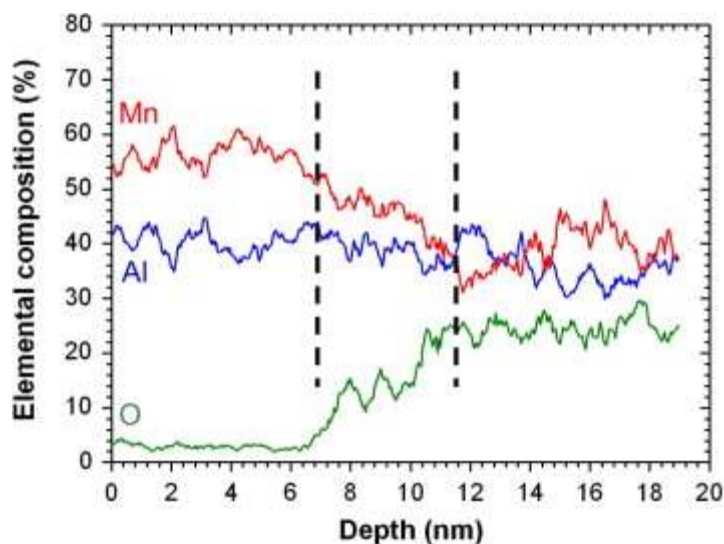
Figure 3.25: Elemental composition profiles of Mn, Al and O elements at an interface between an oxidized region and a non-oxidized region in the milled sample (the corresponding region is displayed by the arrow in figure 3.24).

This further suggests that oxidation does not contribute to the formation of the β-Mn phase, as the β-Mn phase compositional regions do not show any oxidation, all oxidation occurs in the compositional regions that are outside the limits of the β-Mn.

In order to determine if site disorder was responsible for the loss of magnetization, a sample was milled for 15 minutes and the intensity ratio $I_{(001)}/I_{(111)}$ was compared to the original intensity. If site disorder increased, then the intensity of the (001) superlattice peak would decrease (relative to the (111) fundamental peak). The peaks were fitted with a Gaussian fit to determine the area. Figure 3.26 shows the XRD data and the Gaussian fits. The intensity ratio of the 15 minute milled sample was virtually identical to the non-milled sample (both 0.6±0.05), indicating that site disorder did not increase upon milling. It should be noted that a ~15% loss in magnetization was observed even with the relatively short-term milling.

	0 min mill	15 min mill
Magnetization emu/g @ 8kOe	58	40
(001) intensity	5.9	5.7
(111) intensity	100.6	93.6
(001)/(111)	0.059	0.061
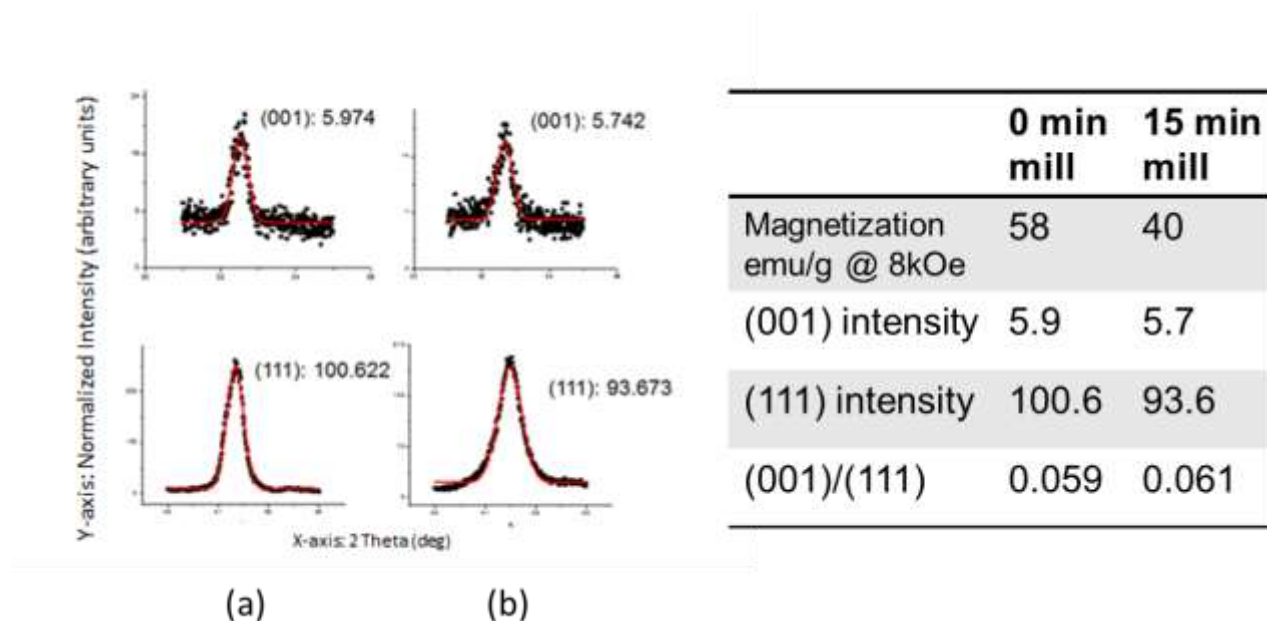
Figure 3.26: Diffraction data and Gaussion fits of the (001) and (111) peaks for (a) unmilled and (b) 15 min milled samples. The numbers shown are areas (in arbitrary units).

With neither oxidation nor site disorder contributing to the loss of magnetization, it appears that the formation of the equilibrium β-Mn (and presumably γ_2 below detection limits) is the predominant contributor. As mentioned, the nominal composition of the alloy lies in the equilibrium phase field of β-Mn+γ_2; thus any decomposition of the metastable τ phase, or equilibrium decomposition of the ε phase, would result in the formation of these phases. Since neither of these phases is ferromagnetic (or ferrimagnetic), then their presence would reduce the phase fraction of the ferromagnetic τ phase, and lower magnetization. Since the high-energy mechanical milling was done using short term (1 minute) intermittent "pulses" to alleviate temperature excursions, the transformation to the equilibrium phases is likely stress-induced. This is similar to what has been observed in other systems, where crystallization of amorphous

structures (i.e., transformation from metastable to stable structures) was stress-induced [42]. The crystallization in this case is thought to be enabled by an increase in defect density [43]. However, it is also probable that some local heating occurred, even with the short-term milling, which assisted in the phase transformation.

ε-phase samples were also mechanically milled using a surfactant (surfactant-assisted mechanically milling). The surfactant eliminates re-welding of fractured particles that occurs during dry milling. This consequently leads to a reduction in particle size[44-48]. Figure 3.27 shows x-ray diffraction patterns of the surfactant-assisted milled samples. The coercivity behavior is similar to the dry-milled samples, with an increase with milling time (Figure 3.19). Here, however, the dramatic loss of coercivity observed in the dry-milled samples does not occur, as a relatively stable coercivity results even for times up to 32 hours [49]. The decrease in magnetization also occurs here.

The morphology of the milled samples was interesting as well. After 10 hours of milling, the particles consisted of very flat platelets with a very high aspect ratio. The thickness of the plates after milling for 10 hours is on the order of tens of nanometers, while the length and width are on the order of several microns (Figure 3.28). Interestingly, the fracture of the particles appears to be mica-like (that is, in sheets). Typically, fracture occurs either transgranular or intergranular. The microstructure (Figure 3.15) consists of predominantly equiaxed grains, so the exact fracture behavior of the melt spun ribbon is not clear. This is in contrast to surfactant-assisted milling studies in other systems, which produced distinct nanoparticles after similar times [U-Y].
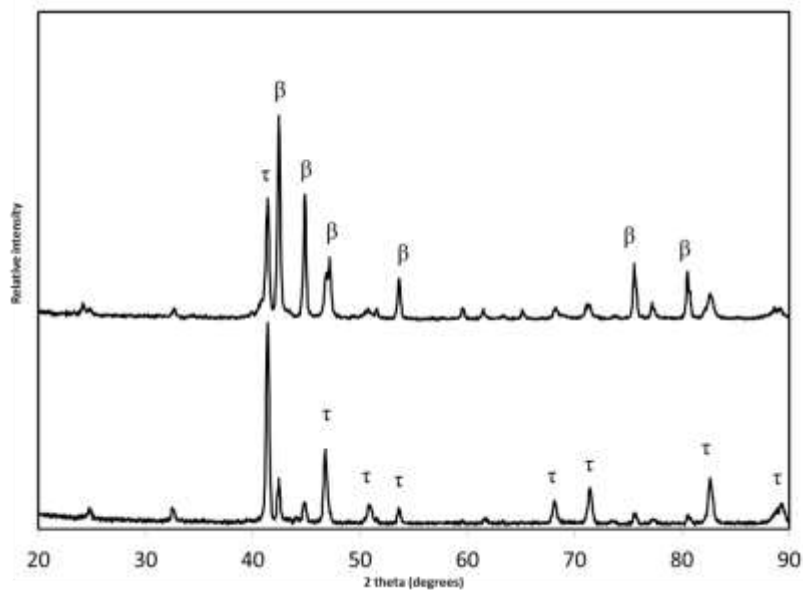
Figure 3.27: X-ray diffraction patterns of surfactant-assisted mechanical milling (SAMM) after (a) half hour, and (b) after 10 hours. SAMM samples also result in the formation of equilibrium phases including β-Mn.
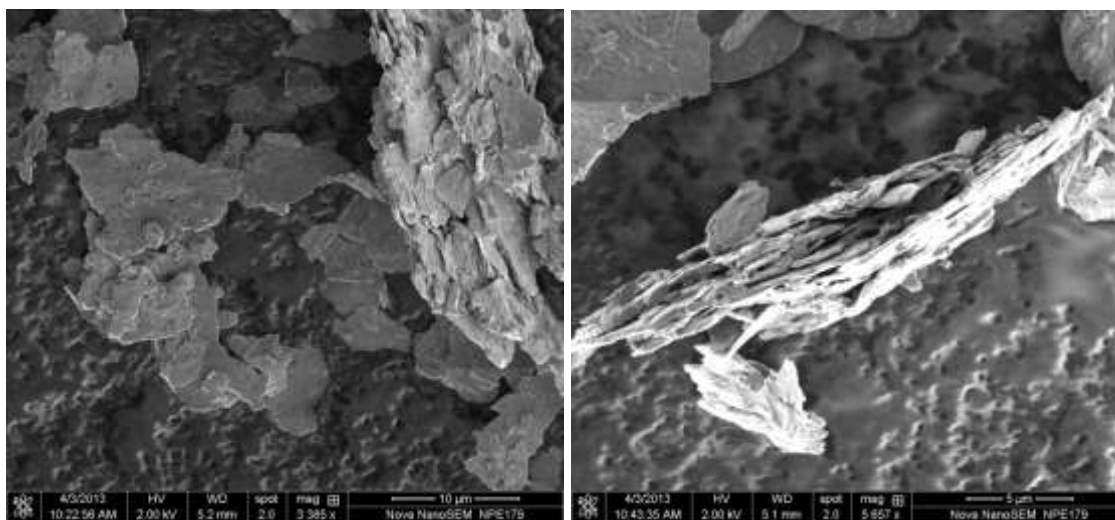
Figure 3.28: SEM of surfactant milled particles

Scanning electron micrograph showing the particle morphology of surfactant-assisted mechanically milled Mn-Al-C particles.

The magnetic properties also showed distinct differences from that of the dry milled samples. The VSM samples were prepared under a magnetic field as discussed in chapter 2. In the as spun and dry milled samples, there was no difference in the hystersis loop whether it was measured along the aligned direction or 90° to this direction. In the surfactant assisted samples, the demagnetization curve along the aligned direction and perpendicular to the alinged direction were different, figure 3.29. When the sample was tested along the aligned direction it demonstrated higher saturation magnetization and higher remanence magnetization suggesting that there existed single crystal particles that were aligned during the sample preparation under the magnetic field. The formation of these single crystal particles is required for the end goal of creating a nanocomposite. In order to for successful exchange coupling, the soft phase must be located between the grains of the Mn-Al phase. By creating Mn-Al particles that are single crystalline, the amount of soft phase that can be effectively exchanged coupled will be maximized.
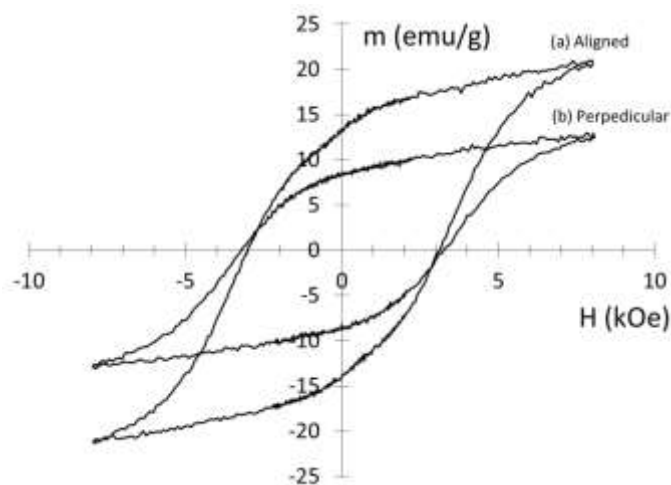
Figure 3.29: 10 hour SAMM magnetic properties

10 hour SAMM magnetic properties measure along (a) aligned direction and (b) at 90° to the aligned axis suggesting the existence of single crystal particles.

4. Hot Pressing

The final processing step for the permanent magnet material is consolidation. Hot pressing of permanent magnets is able to create fully dense magnets that generate the highest energy products. The material was hot pressed at the GM research center in Warren, Michigan. The initial sample was milled for a 30 minutes in the τ phase, and then was sent for compaction. Two samples were pressed at a force of 20kN for 8 min, one at 700°C and one at 800°C. The resulting magnets are shown in figure 3.30. The end product had an outside diameter of 0.5 inches and a height of 0.2 inches.

Figure 3.30: Hot pressed Mn-Al samples

Both the density and magnetic properties varied with the consolidation temperature. The density of the sample pressed at 800°C was 99.50% dense, while when pressed at 700°C the density was 98.20%. The magnetic properties also varied with temperature. The magnetic properties are listed in table 3.2.

UNL processing	description of GM compression	% of density compaction	B_r (kG)	H_{ci} (kOe)	BH_{max} (MGOe)
Mn$_{54}$Al$_{43}$C$_3$ milled for 1 hr in τ	800C, 20 kN for 8 min	99.50%	1.769	1.035	0.39
Mn$_{54}$Al$_{43}$C$_3$ milled for 1 hr in τ	700C, 20 kN for 8 min	98.20%	1.253	1.9	0.29

Table 3.2: description of τ milled sample properties after compaction

From table 3.2 it can be seen that the sample pressed at the lower temperature has a higher coercivity. This can be attributed to the higher temperature processing causing grain growth. Despite the 700°C sample being pressed at a lower temperature it had a lower energy product. This is because of the lower magnetization, and is primarily due to phase change since the decrease in density is not enough to account for the full change in B_r. From the XRD patterns for the samples taken after compaction (figure 3.31) the change in magnetization is due to the formation of equilibrium phases.
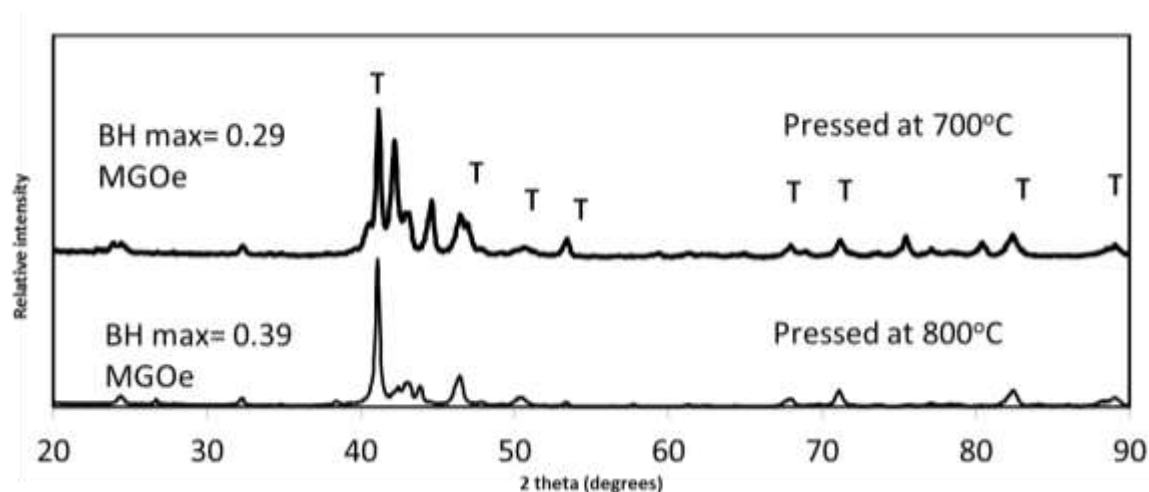
Figure 3.31: XRD patterns for compacted sample of τ-milled powders

With the realization of the improved magnetic properties of the ε milling samples milled in the ε phase milled samples were compacted next. Since the hot pressing temperatures are above the 500°C required for the annealing, the annealing and compaction steps could be combined into one process, an important study for the industry partners. First a study was done to show that the cooling rate from the ε to τ transition did not have an effect on the structure or properties of the materials. Figure 3.32 shows the XRD patterns for samples cooled at three different rates. There was no change in the structure or properties due to the changes in cooling rates.
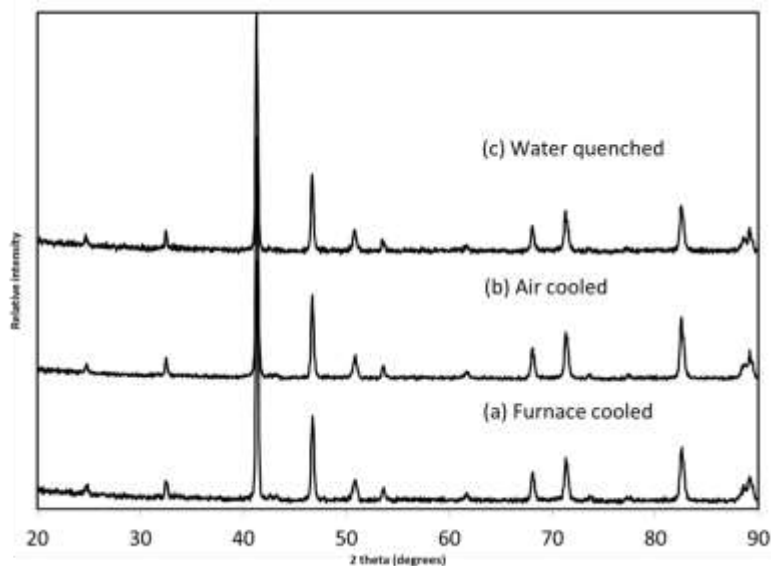
Figure 3.32: Mn54Al43C3 samples cooled at different rates from the 500oC annealing step.

Since there was no change in properties due to the cooling rate powder that was milled for 30 min in the ε phase was sent to GM to be hot pressed and transformed to τ in a single step. Two different alloys were sent, the original $Mn_{54}Al_{43}C_3$ alloy and the $Mn_{51}Al_{43}C_3Cu_3$ alloy. The goal was to have some of these samples pressed at a lower temperature that would not induce the grain growth seen in the previous samples and maintain the coercivity of the fine grained powders. While the addition of Cu negatively impacts the magnetic properties, its ability to ease consolidation might result in an overall benefit. A description of these samples and their properties are shown in table 3.3.

composition	description of GM compression	% of density compaction	B_r (kG)	H_{ci} (kOe)	BH_{max} (MGOe)
$Mn_{54}Al_{43}C_3$	800C, 20 kN	98%	1.891	1.12	0.454
$Mn_{54}Al_{43}C_3$	600C, 20 kN	83%	2.319	2.273	0.934
$Mn_{54}Al_{43}C_3$	650C, 20kN	92%	1.971	2.262	0.686
$Mn_{51}Al_{43}C_3Cu_3$	600C, 20 kN	90%			

Table 3.3: Descriptions of samples compacted in the ε phase.

The ε milled samples had higher B_r values then that of the τ milled samples due to the higher

phase fraction of magnetic τ phase. Hot pressing at lower temperatures, 600°C and 650°C,

resulted in higher coercivities suggesting that this temperature is not high enough to cause grain

growth in the material. However, pressing at these lower temperatures did result in less dense

magnets. The addition of 3% Cu did increase the compaction density by 9% at 600°C due to the

lowering of deformation resistance discussed in [41].

The reversibility of the phase changes during processing was investigated as well. The

consolidated magnet was heat treated at 1050°C for 10 minutes in Ar, similar to that of the

powders. However since the consolidated magnet could not be sealed, it was annealed in a tube

furnace under argon atmosphere, removed and briefly exposed to air, then oil quenched instead

of water quenched. XRD patterns and hysteresis loops show that the reversal to ε phase and

again to τ is possible even in the consolidated state. The XRD patterns showing the full

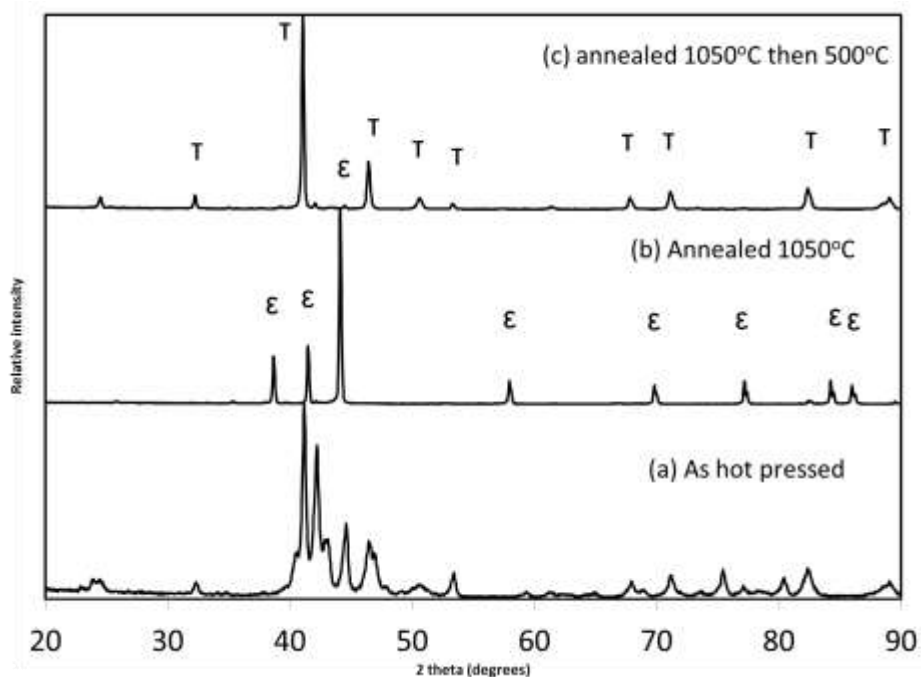reversibility of the phase changed in the compacted sample is shown in figure 3.33.

Figure 3.33: Compacted sample annealed back to ε and then τ.

After this annealing treatment the energy product increased from 0.29 MGOe to 0.98 MGOe.

This was due to an increase in B_r from 1.253 kG to 2.873 kG, which can be attributed to the

increase in phase fraction of the τ phase after the annealing (figure III-36). However the

coercivity decreased from 1.9 kOe in the as pressed sample to 1.39 kOe in the annealed sample

as the microstructure refinement achieved during milling was not maintained by the high

temperature heat treatments similar to the results seen in figure 3.21 and figure 3.20. The values

can been found in table 3.4.

	% of density compaction	B_r (kG)	H_{ci} (kOe)	BH_{max} (MGOe)
As hot pressed, before annealing	98.20%	1.253	1.9	0.29
Hot pressed then annealed		2.837	1.388	0.9792

Table 3.4: Comparison of magnetic properties before and after annealing of compacted sample

5. Conclusions

From these experiments it can be concluded that $Mn_{54}Al_{43}C_3$ is the optimum composition

for τ phase formation. Ni, Co, and Ti prevented the formation of the τ phase. Samples with Fe

and Cu additions successfully formed the τ phase, but the addition of these elements lowered the

saturation magnetization and anisotropy constants of the material. Both the $Mn_{48}Al_{43}C_3Fe_6$ alloy

and the $Mn_{51}Al_{43}C_3Cu_3$ maintained the same remanent magnetization as the original $Mn_{54}Al_{43}C_3$

sample with no alloying additions. All Cu- substituted samples had lower coercivities then that

of the $Mn_{54}Al_{43}C_3$ and Fe-substituted samples. Mechanical milling of Mn-Al-C is an effective

way of increasing coercivity; however, it results in the formation of equilbrium phases,

specifically the β-Mn phase with a composition close to Mn_3Al_2, that reduces the magentization

and energy product. This loss in magnetization was not from oxidation or site disorder, but

changes in phase constitution. Milling in the ε phase followed by conversion to τ significantly

reduced the amount of equilbrium phase formed. Surfactant-assisted milling showed similar

equilbrium phase formation but resulted in a unique powder morphology, platelets, and was able

to form single crystal particles that could be aligned into an anisotropic magnet. Mn-Al can be

condensed to fully dense magnets via hot pressing at temperature of $700^{o}C$ and above; however,

this results in grain growth and negates any microstructure refinement achieved through

mechanical milling. Hot pressing at lower temperatures resulted in a magnet that was less dense

but retained the coercivity of the milled powders. However, the addition of small amounts of Cu

increased the density. Finally, hot pressing of ε powders consolidates and transforms it to the τ

phase in a single processing step. Samples with a coercivity as high as 4.6 kOe were created.

Powders were condensed to fully dense isotropic magnets with a maximum energy product of

0.98 MGOe.

IV.   Zr-Co

1. Background

Zr-Co is another material that has shown promise as a rare-earth free permanent magnet.

The composition of interest is the Zr_2Co_{11} composition. The Zr-Co phase diagram is shown in

figure 4.1. The exact structure of this phase is still under study, although sources index it as

orthorhombic, rhombohedral, cubic, or a combination thereof [19-21, 26]. It has hard magnetic

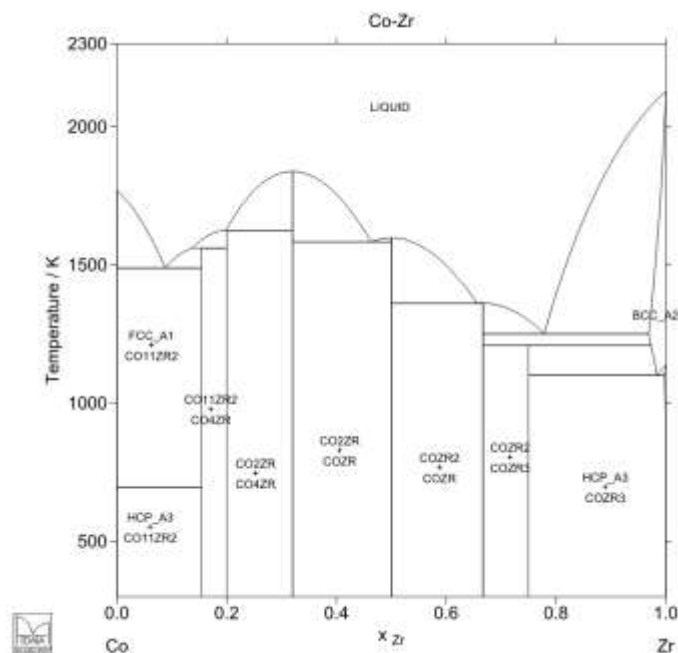properties with energy products as high as 4.6 MGOe [18].

Figure 4.1: Zr-Co phase diagram

From [51].

Similar to Mn-Al, rapid solidification is commonly used to form these alloys. The previously

mentioned studies claim a combination of the Zr_2Co_{11} phase with either Co or the Zr_6Co_{23} phase

[18-21,26]. Pure cobalt forms either a FCC or HCP phase with high magnetization, 143 emu/g at

saturation [50], and low anisotropy. The Zr_6Co_{23} phase is a cubic phase with magnetization of 67

emu/g at 8 kOe and similarly low anisotropy. For use in nanocomposites, it is important that the

magnetically-hard Zr_2Co_{11} phase be isolated and processed to a favorable microstructure. The

study by W.Y. Zhang et al.[18] showed that the optimal composition for Zr_2Co_{11} formation as

well as the highest energy product occurs at $Zr_{18}Co_{82}$. It was also shown that Zr_2Co_{11} phase

fraction increased with wheel speed up to 45 m/s, which was the maximum value tested. The

hysteresis loops displayed single-phase behavior, suggesting that the phases are mixed on the

nanoscale resulting in coupling of the hard and soft phases [18]. In a similar study performed by

A.M. Gabay et al. [20] that found $Zr_{16.4}Co_{83.6}$ to be the optimal composition for Zr_2Co_{11} formation. The addition of Mo was found to increase the coercivity but also decreased the magnetization and energy product [21]. In this thesis, the physical metallurgy of the Zr-Co alloy will be studied in an attempt to optimize magnetic properties. Following this, processing will be done to attempt to prepare the alloy for hot pressing and consolidation into fully dense permanent magnets.

2. Physical Metallurgy

First samples were created at the two compositions that were found to be the most favorable for Zr_2Co_{11} formation, $Zr_{16}Co_{84}$ and $Zr_{18}Co_{82}$. The hysteresis loops of these samples are shown in figure 4.2. The high magnetization as well as what appears to be two phase behavior, a small kink appears around the field of 0 kOe, in the $Zr_{16}Co_{84}$ alloy suggests the presence of a large amount of a soft magnetic Co-rich phase.
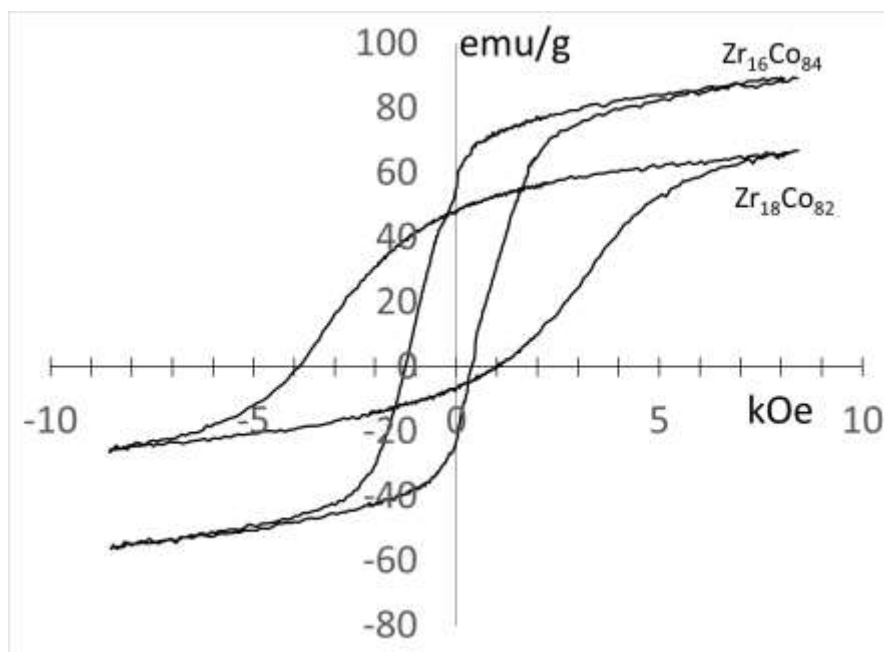

Figure 4.2: Hysteresis loops for $Zr_{16}Co_{84}$ and $Zr_{18}Co_{82}$

The presence of the additional peak in the XRD pattern for the $Zr_{16}Co_{84}$, figure 4.3, also suggests the formation of the Co phase (indexed as HCP-Co in [18] and FCC-Co in [21]) in this sample. Due to the peak position, it is possible that Zr is dissolved into the Co-rich phase causing the peak to shift to a lower angle than normal for the HCP-Co or FCC-Co phase. Alternatively there could exist multiple phases at the Zr_2Co_{11} composition and that the ratio at which these two phases form is heavily influenced by the starting composition and cooling rate. The difficulty in producing rapid solidification results at this composition with identical magnetic properties and diffraction patterns would further support this theory of isocompositional structural changes at the Zr_2Co_{11} composition. Two peaks labeled "A" and "B" can be seen in figure 4.3. Peak "A" corresponds to the magnetically hard phase, peak "B" corresponds to the second unidentified phase with low coercivity and high magnetization. Peak "B" is shifted too far to be either a Zr-substituted HCP or FCC Co phase and most likely represents a second structure at the Zr_2Co_{11} composition, however this phase cannot be indexed to any pattern in the "International Centre for Diffraction Data" database due to the multi-phase nature of the sample and lack of additional peaks.
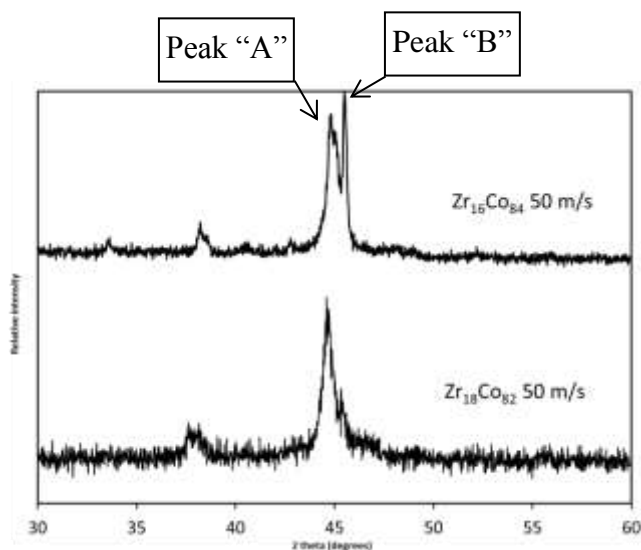

Figure 4.3: XRD patterns for $Zr_{16}Co_{84}$ and $Zr_{18}Co_{82}$

The research by Zhang et al. [18] showed an increase in coercivity with increasing wheel speed up to the highest tested value of 45 m/s. At 45 m/s a coercivity of 3.0 kOe and an energy product of 4.8 MGOe were reported. In this thesis, wheel speeds of 50 m/s and 55 m/s were used to produce the alloys. Samples produced with a wheel speed of 50 m/s had coercivity of 3.9 kOe and energy product of 3.6 MGOe. This supports the previous work that showed increasing coercivity but decreasing magnetization with an increase in wheel speed. This is most likely from a reduction in the amount of Co-rich phase being formed as wheel speed was increased. At a wheel speed of 55 m/s, the coercivity was lower than that in the sample made at a wheel speed of 50 m/s (figure 4.4). 50 m/s was chosen as the wheel speed for the remainder of this thesis, as it resulted in the highest coercivity and what is assumed to be the closest to single phase of all the samples due to its high coercivity and low magnetization.
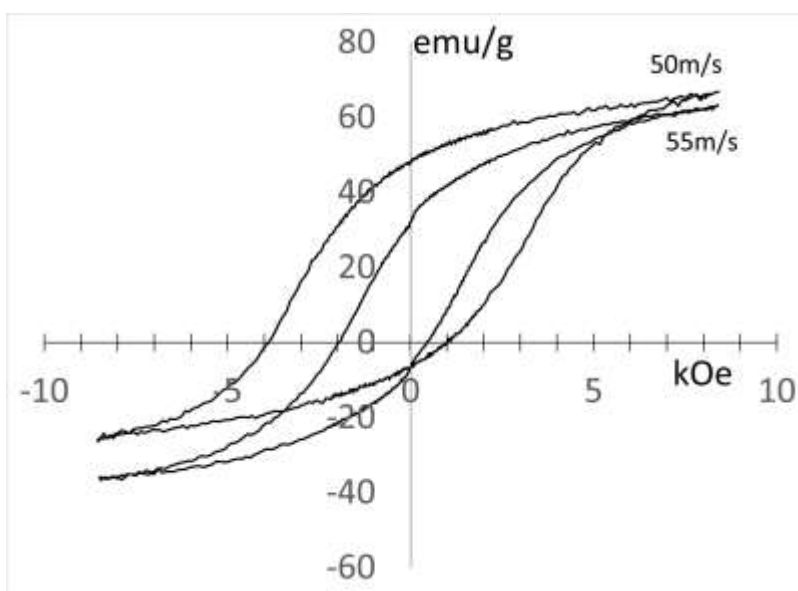

Figure 4.4: Hysteresis loops for 50 m/s and 55 m/s.

The addition of Mo, Si, and B has shown to increase the coercivity of the alloy [21]. This alloy was investigated as well since it could react differently to milling or heat treatments and may be

more stable than the original Zr-Co alloy. The $Zr_{16}Co_{73}Mo_5Si_3B_3$ composition from [21] was made. A second sample was formed assuming that Mo atoms would substitute for the Zr; the alloy formula was then $Zr_{12}Co_{77}Mo_5Si_3B_3$. When melt spun at a wheel speed of 50 m/s, these alloys had poor magnetic properties; however, at 10 m/s the coercivities were higher than that of the $Zr_{18}Co_{82}$ alloy (figure 4.5). As the amount of Zr and Mo, the two period 5 elements, to Co $(\frac{Zr+Mo}{Co})$ increases, so does the coercivity, while the magnetization decreases.
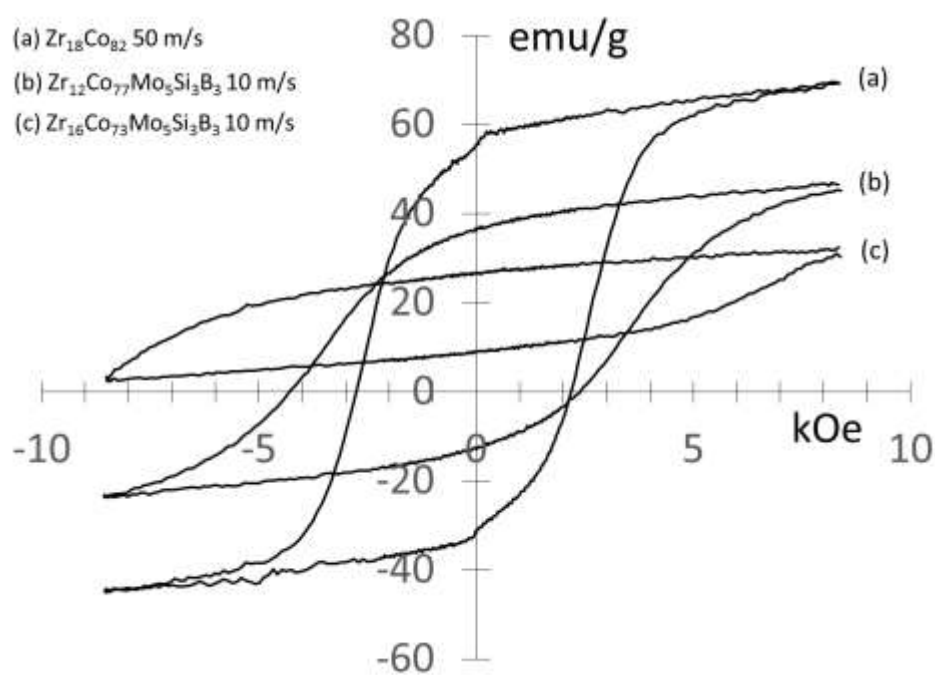
Figure 4.2: M-H loops for Mo-Si-B addition

This increase in coercivity would appear to be due to chemistry, either the increased period 5 elements concentration or the Si-B addition, and not the microstructure. Figure 4.6 shows TEM images of the $Zr_{18}Co_{82}$ alloy and the $Zr_{12}Co_{77}Mo_5Si_3B_3$ alloy. From these images it can be seen that the compositional changes do not induce grain refinement, and that the grain size in both samples is around 100nm.
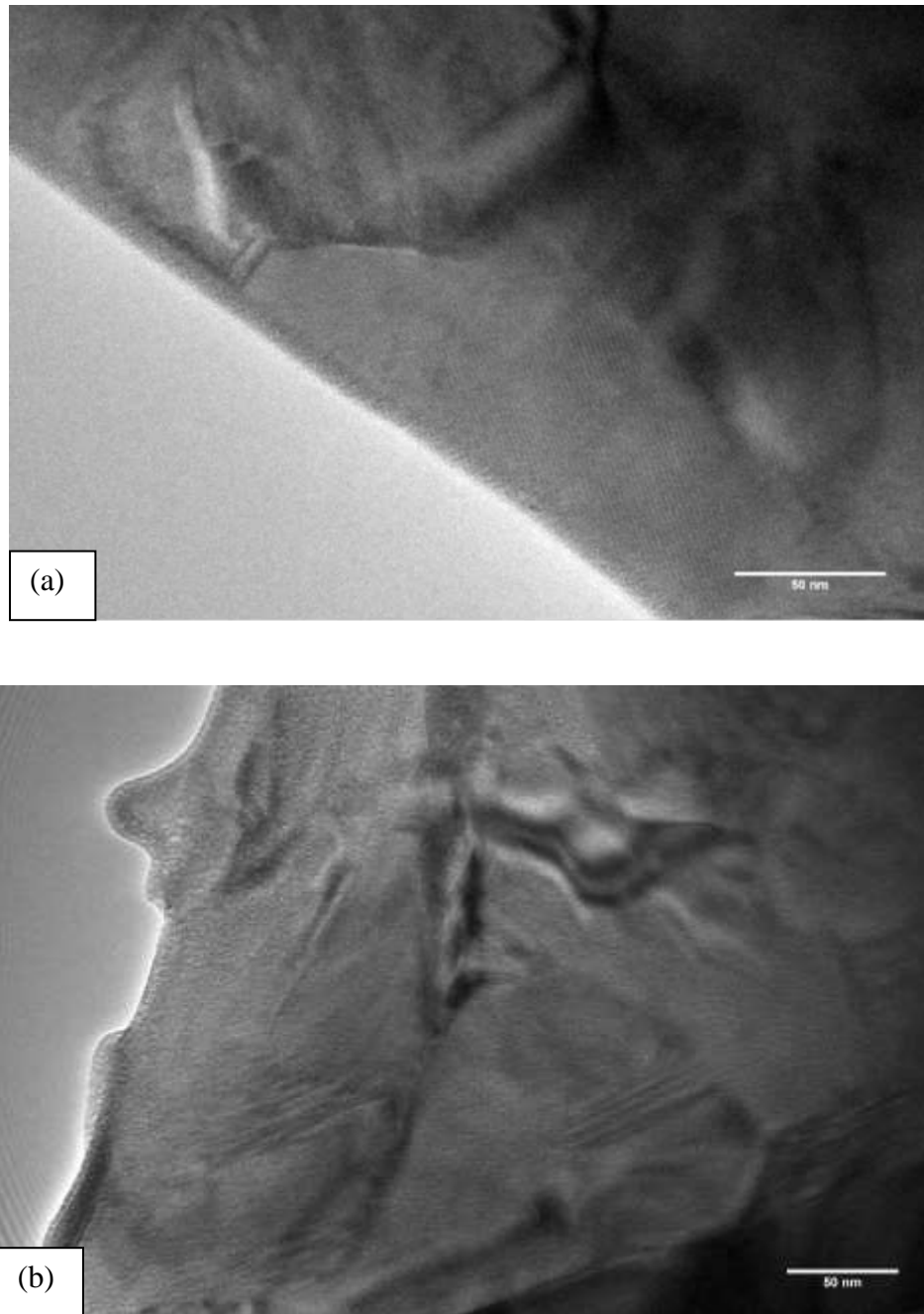
Figure 4.3: TEM images of (a) $Zr_{18}Co_{82}$ and (b) $Zr_{12}Co_{77}Mo_5Si_3B_3$

The M-H hysteresis loops for these samples show an increase in coercivity but loss in

magnetization. Figure 4.7 shows the B-H loops for this material, it can be seen that despite the

increase in coercivity, the addition of Mo-Si-B decreases the energy product.
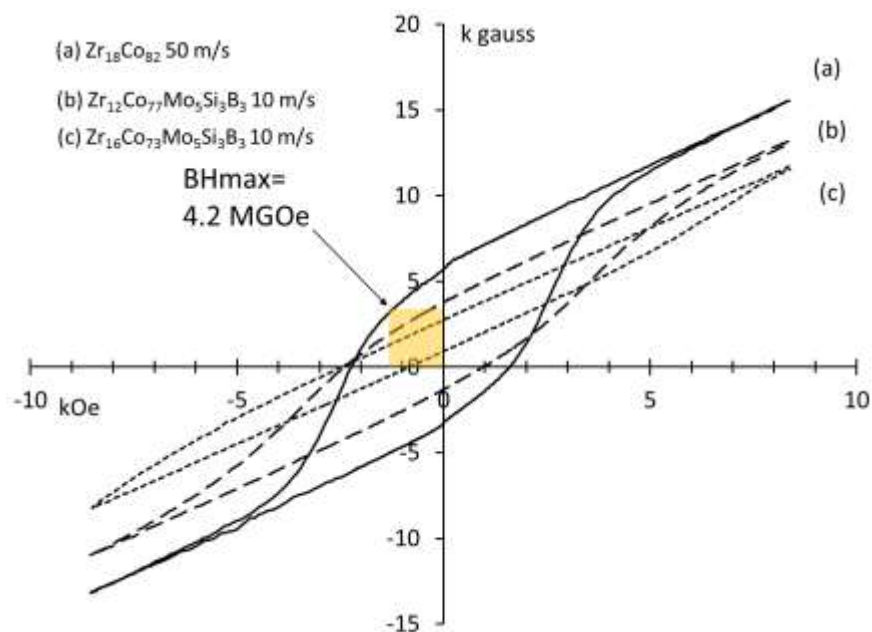
Figure 4.4: B-H loops for Zr-Co and Zr-Co-Mo-Si-B

3. Mechanical Milling

The end goal of this study is to create an anisotropic permanent magnet and exchange coupled nanocomposites. Therefore it is important to first create single crystal particles of the hard magnetic phase. By creating single crystal particles, these particles can then be aligned along their c-axes and consolidated to create the anisotropic magnet with increased energy product. In the nanocomposites, the soft phase must be bordered by hard phase grains. Having single crystal hard phase particles makes this intimate mixture possible. The fracture surface was investigated via SEM. In order to create an anisotropic magnet at low temperatures the material must be fractured along the grain boundaries resulting in single crystal particles that can be aligned during consolidation. The fracture surface of the melt spun ribbons showed symptoms of intergranular fracture. This is based on the granular nature of the surface and lack of planar fracture surfaces (figure 4.8).
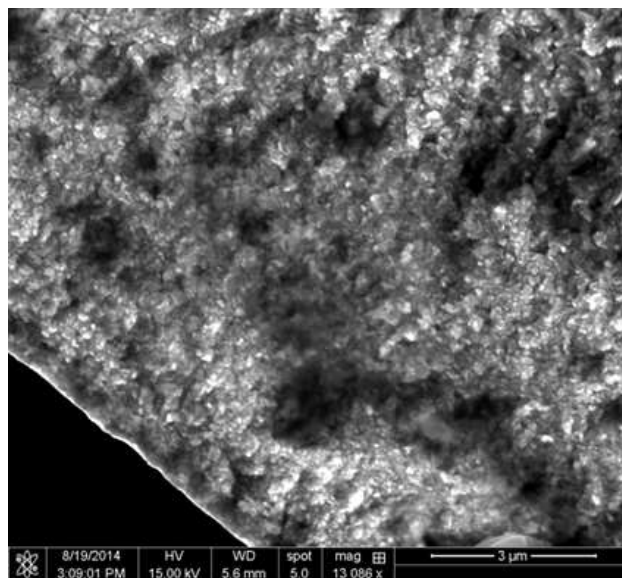
Figure 4.5: Fracture surface of $Zr_{18}Co_{82}$ **ribbons**

This is in contrast to the $Zr_{16}Co_{84}$ alloy that demonstrated different fracture mechanics.

Whereas the $Zr_{18}Co_{82}$ alloy was brittle, the $Zr_{16}Co_{84}$ alloy exhibited ductile behavior when

broken. The SEM images of the $Zr_{16}Co_{84}$ fracture surface reflected this ductile behavior (figure

4.9). This ductile behavior is most likely due to the Co-rich metallic phase.

Figure 4.6: Fracture surface of $Zr_{16}Co_{84}$ **ribbons**

Surfactant assisted milling was performed on the $Zr_{18}Co_{82}$ alloy in an attempt to increase coercivity and create single crystal particles for compaction. Surfactant assisted milli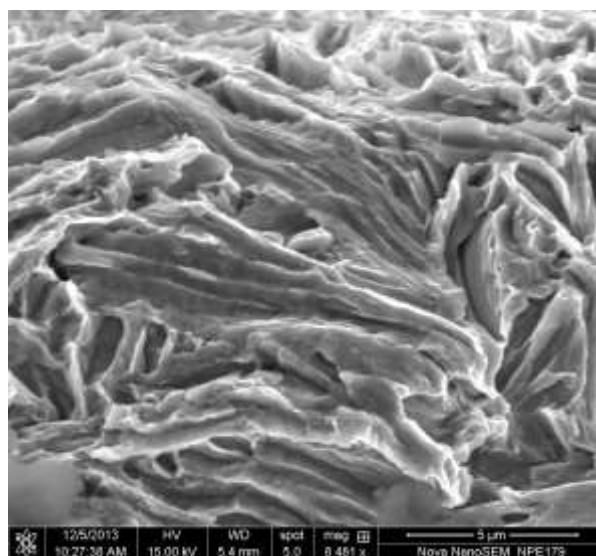ng was selected to avoid the rewelding of particles that would create multi-crystal particles. The sample was milled for one hour using oleic acid as a surfactant. Milling of the sample resulted in a loss of coercivity, although the sample maintained a magnetization of around 65 emu/g at 8 kOe (figure 4.10). The hysteresis loop for the milled sample showed two phase behavior, suggesting the formation of the Zr_6Co_{23} phase that would have similar magnetization but low coercivity.
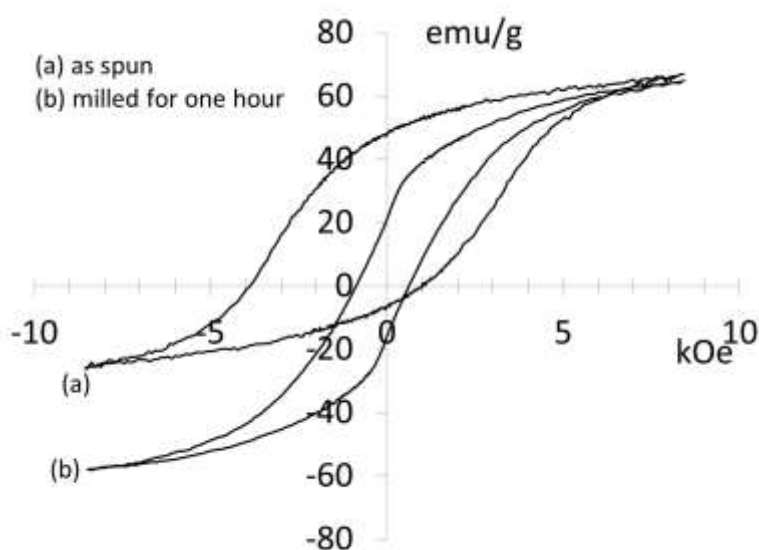

Figure 4.7: $Zr_{18}Co_{82}$ 50 m/s hysteresis loops before and after one hour surfactant milling. Similar to the stress induced phase transformation in the Mn-Al, there is a phase change that occurred when milling the Zr-Co sample. However, unlike the Mn-Al alloy, this transition is not to a non-magnetic phase but rather a softer magnetic phase. The XRD pattern post-milling shows broadening of the peaks as well a shift of the center of the peak to a higher angle (figure 4.11). This shift of the primary peak could be the formation of a second more stable phase similar to that found in the Mn-Al. These theories are supported by the XRD pattern after the sample is annealed at 500°C. In this pattern the Zr_6Co_{23} phase {511} peak becomes evident. This combined

with the {440} peak, which overlaps with the Zr_2Co_{11} phase, suggests that the Zr_6Co_{23} phase is formed during the milling, or that an amorphous phase is forming that is then converted to the Zr_6Co_{23} phase during the annealing treatment. In both of these cases it suggests that the Zr_2Co_{11} phase is a metastable phase and that the Zr_6Co_{23} phase is the more stable structure. This is also supported by the magnetic measurements, as the magnetization of the Zr_6Co_{23} phase is similar to that of the Zr_2Co_{11} phase, the creation of Zr_6Co_{23} should not adjust the magnetization of the material at 8 kOe (figure 4.10).
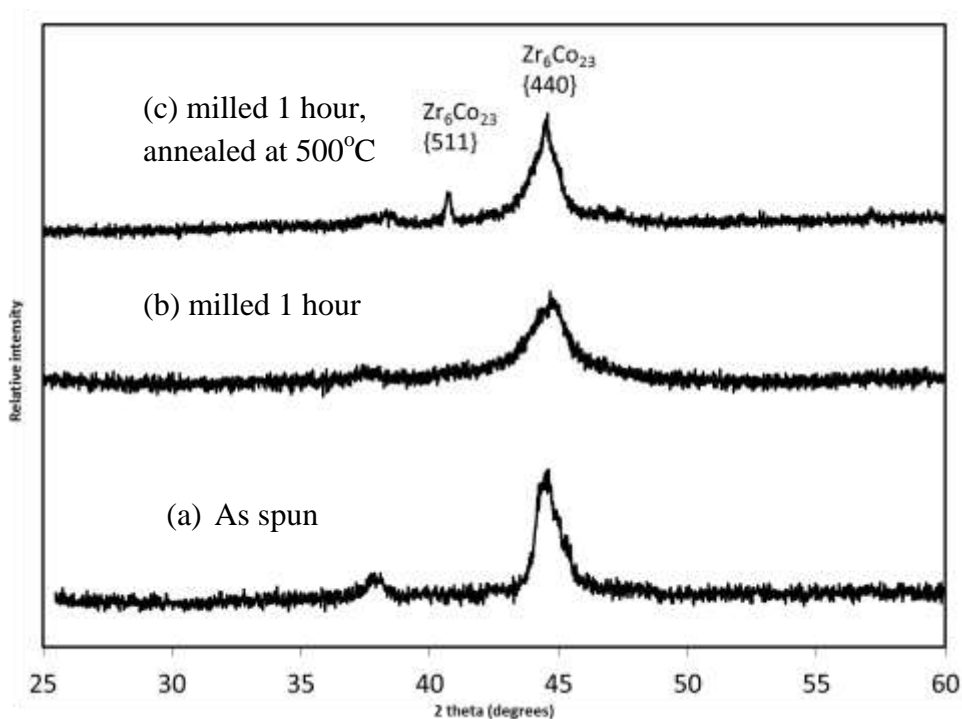

Figure 4.8: $Zr_{18}Co_{82}$ milled XRD patterns. (a) as spun sample, (b) sample milled 1 hour with surfactant, (c) milled 1 hour then annealed at 500^oC for 10 minutes

Similar to the surfactant milled Mn-Al sample, Zr-Co surfactant assisted milling resulted in plate-like particles with high aspect ratios (figure 4.12).
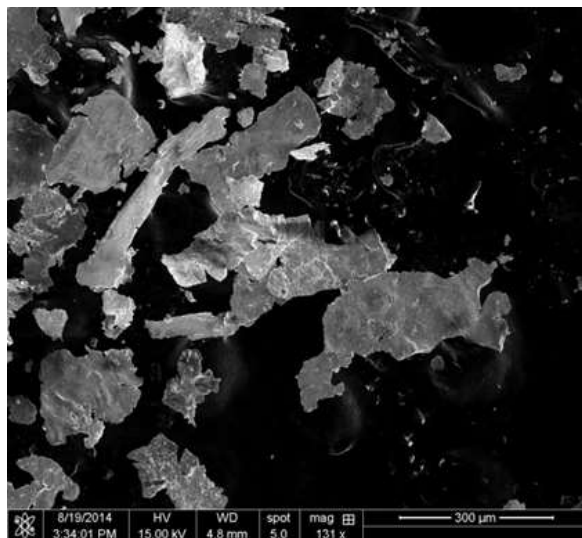
Figure 4.9: SEM image of surfactant assisted milled Zr-Co

4. Compaction

i. Hot Press Applications

In chapter 3, it was shown that the high temperature required for hot pressing caused grain growth and any microstructure refinement gained during milling to be lost. The as spun Zr-Co samples do not require further grain refinement due to the initial high coercivity. However due to what appears to be the metastable nature of the magnetically hard Zr_2Co_{11} phase, it may face similar issues of phase transformation. The $Zr_{18}Co_{82}$ sample was melt spun at 50 m/s and then annealed at 500^oC, 600^oC, and 700^oC for 10 minutes. Starting at 600^oC, the Zr_6Co_{23} {511} becomes visible in the XRD pattern (Figure 4.13). As the annealing temperature is increased this peak becomes more intense, suggesting a larger phase fraction of the Zr_6Co_{23} phase.

Figure 4.10: XRD pattern for heat treated $Zr_{18}Co_{82}$ 50 m/s. (a) as spun sample, (b) sample annealed at 500^oC, (c) sample annealed at 600^oC, (d) sample annealed at 700^oC

Hot pressing the $Zr_{18}Co_{82}$ alloy at temperatures sufficient for densification would be problematic, as heating to this temperature induces the formation of the Zr_6Co_{23} phase. The formation of this second phase results in a two phase hysteresis loop with a low energy product. The magnetic properties of these annealed samples are shown in figure 4.14.

Figure 4.11: Hysteresis loops of $Zr_{18}Co_{82}$ melt spun ribbons. (a) as spun sample, (b) sample annealed at 500°C, (c) sample annealed at 600°C, (d) sample annealed at 700°C

The thermal stability of the $Zr_{16}Co_{73}Mo_5Si_3B_3$ alloy was also tested. This alloy showed the same phase decomposition as the binary Zr-Co alloy (figure 4.15). The hysteresis loops showed similar decoupling and two phase behavior, with the two phase behavior starting after the heat treatment at 500°C sample (figure 4.16).
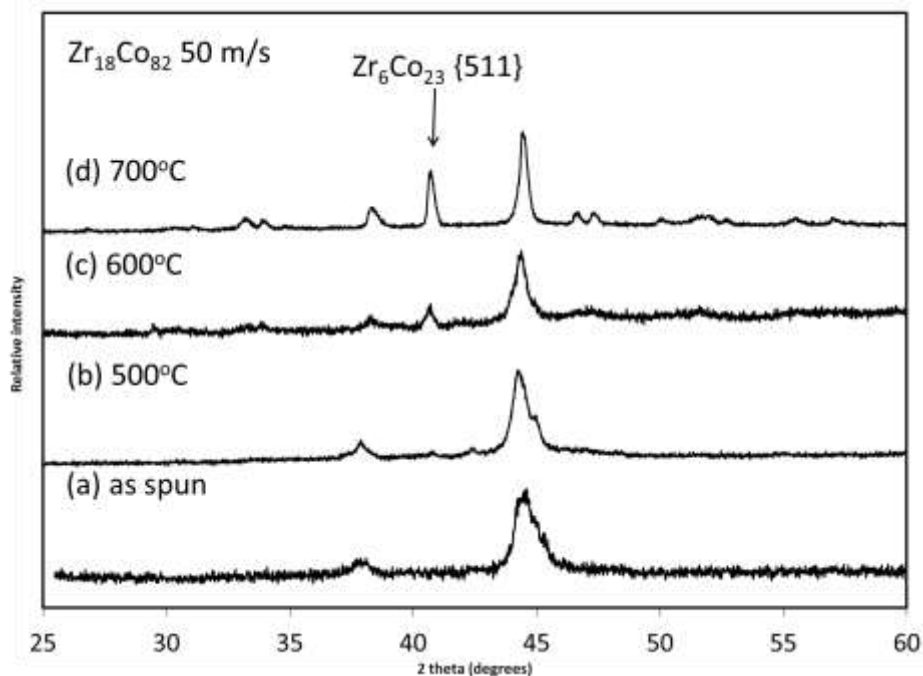
Figure 4.12: XRD patterns for heat treated $Zr_{16}Co_{73}Mo_5Si_3B_3$. (a) as spun sample, (b) sample annealed at 500^oC, (c) sample annealed at 600^oC, (d) sample annealed at 700^oC
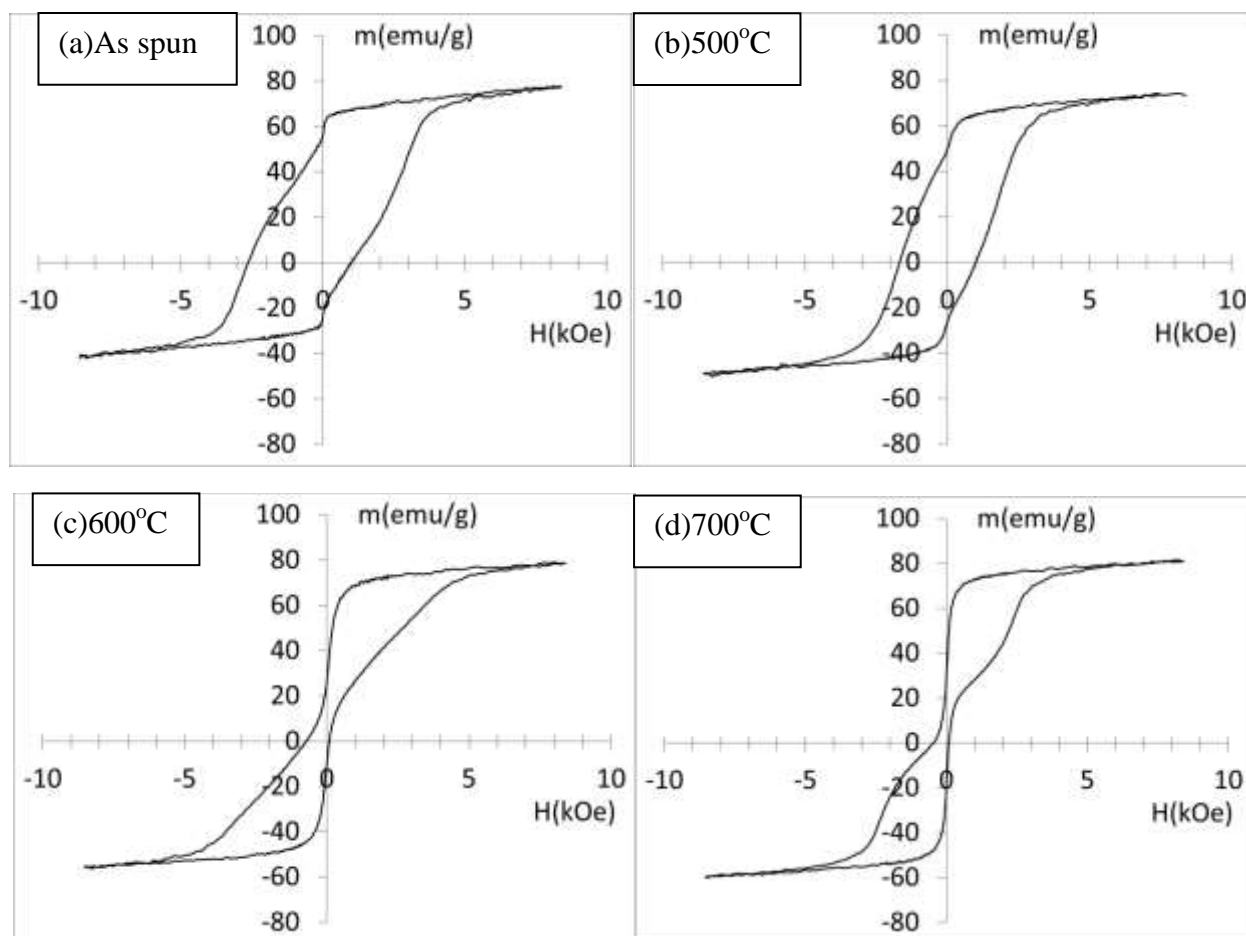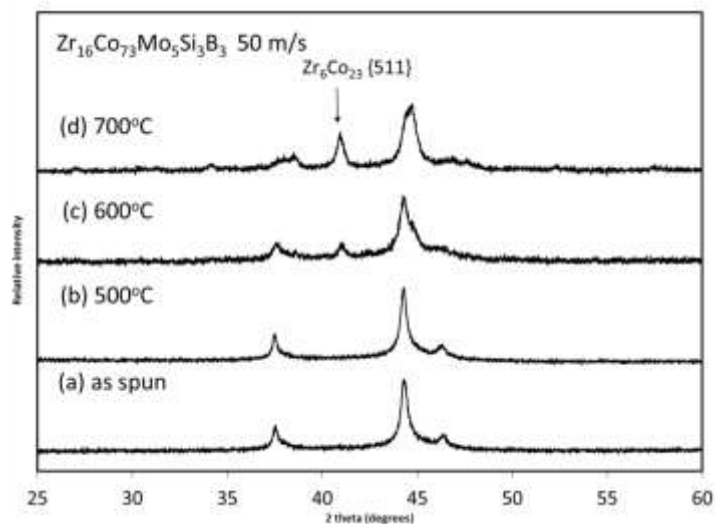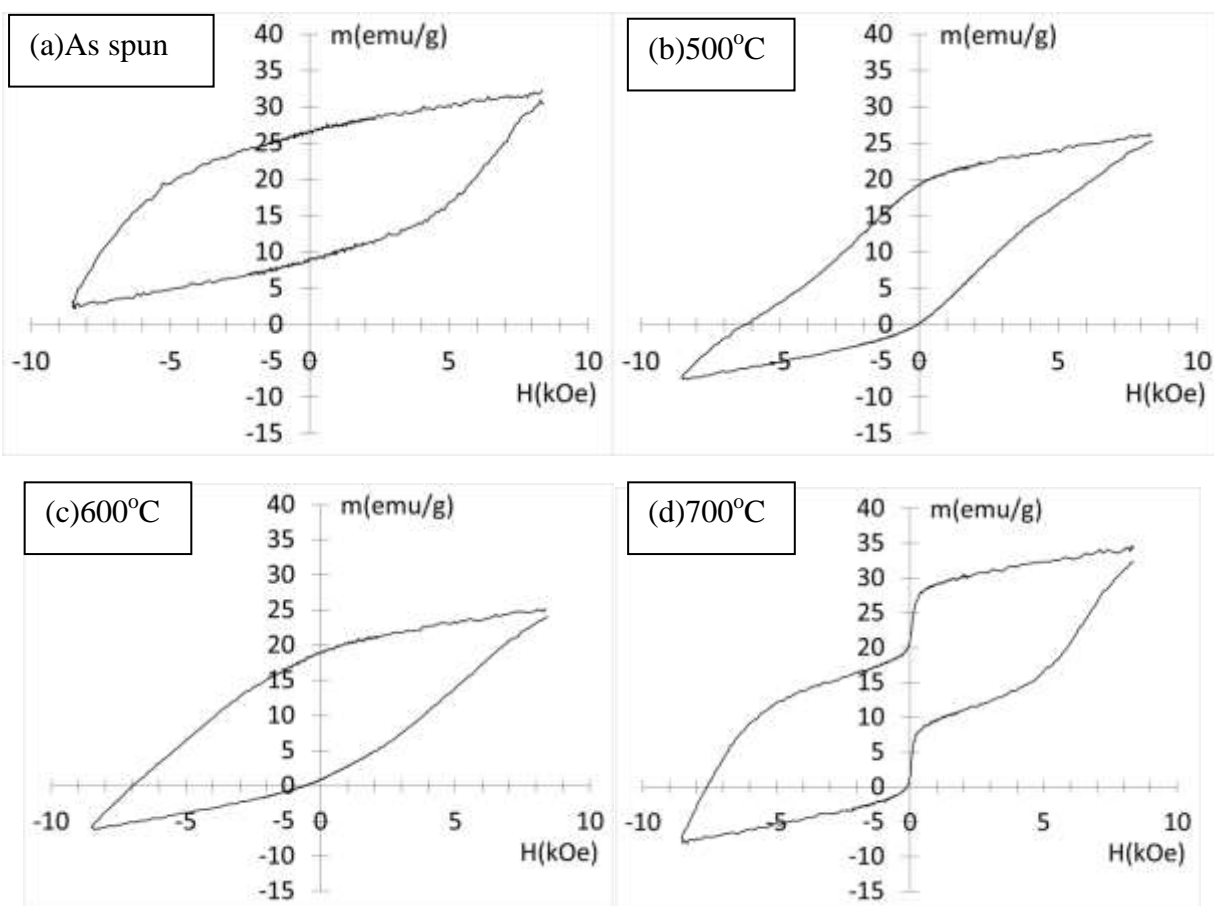

Figure 4.13: Hysteresis loops of $Zr_{16}Co_{73}Mo_5Si_3B_3$ melt spun ribbons. (a) as spun sample, (b) sample annealed at 500^oC, (c) sample annealed at 600^oC, (d) sample annealed at 700^oC

ii.   Hydrogen Embrittlement

Because the formation of the Zr_6Co_{23} phase occurs at heat treatment temperatures as low as 500^oC, hot pressing to form anisotropic Zr-Co magnets is not a viable option. However if single crystal particles can be synthesized, these particles could be aligned by a magnetic field and condensed at lower temperatures that do not involve the high temperatures of traditional hot pressing to induce anisotropy. Hydrogen embrittlement is a common problem in steels when processed in hydrochloric acid. Hydrogen embrittlement involves the collection of hydrogen ions along grain boundaries which causes fracture along the grain boundaries. Hydrogen embrittlement could be used to encourage fracture along the grain boundaries of magnetic materials to aid in the formation of singe crystal particles and avoid the formation of amorphous material seen in mechanical milling. Zr-Co samples were processed in HCL solutions, aligned, and their magnetic properties measured along the easy and hard axis (figure 4.17). The samples showed significant M_r enhancement, 17% alignment, and no loss in saturation magnetization. The acid embrittled sample showed a reduction in coercivity and, as a result, energy product. This is due to the development of texture of the sample as well as the loss of the smaller grain particles, as they were dissolved by the acid. This study demonstrates that grain boundary embrittlement through hydrogen embrittlement could be an effective way of creating aligned permanent magnets; however, the acid concentration and time parameters must be optimized in the future to avoid the loss of material, specifically the smaller particles that tend to be single crystalline.

80 — m(emu/g)

Solid line: (001)
Dashed line: (100)
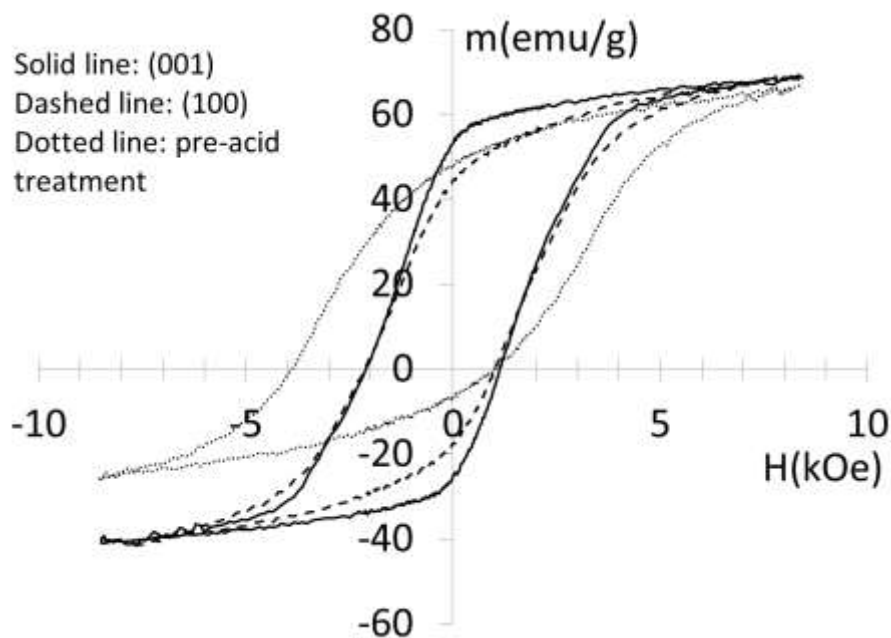Dotted line: pre-acid treatment

Figure 4.14: Aligned Zr-Co magnets formed through hydrogen embrittlement Solid line: post acid treatment (001) direction, dashed line: post acid treatment (100) direction, dotted line: pre-acid ribbon

5. Conclusions

Due to the high coercivity and good magnetization, Zr-Co is a strong candidate as a permanent magnet material. However, the lack of knowledge about the crystal structure at the Zr_2Co_{11} composition makes the study of this material challenging. The $Zr_{18}Co_{82}$ spun at wheel speeds of 50 m/s resulted in a coercivity as high as 3.9 kOe and energy product as high as 4.2 MGOe. The coercivity of the alloy can be increased with the addition Mo-Si-B but this addition decreases the energy product due to the lower saturation magnetization. Both of these alloys undergo phase decomposition during heat treatments at temperatures as low as $600^{o}C$ to the Zr_6Co_{23} phase. This is in contrast to the phase diagram that claims the Zr_2Co_{11} phase to be stable from $1500^{o}C$ until melting. A similar phase transformation was seen during mechanical milling

of the $Zr_{18}Co_{82}$ alloy. Because of these phase transformations during annealing and milling,

traditional hot pressing does not pose an effective way to create fully dense Zr-Co permanent

magnets. However hydrogen embrittlement of the alloy using HCl was able to achieve single

crystal particles that could be used to create an anisotropic magnet. Further studies are needed to

optimize this process of creating single crystal particles and ways to consolidate them into fully

dense magnets without the assistance of high temperatures. The single crystal Zr-Co particles

could then be used in exchange coupled nanocomposites with a high magnetization material such

as Fe-Co.

References

[1] N. Poudyal, J.P. Liu. J. Phys D: Appl. Phys. **46** (2013).

[2] O. Gutfleisch, M.A. Willard, E. Bruck, C.H. Chen, S.G. Sankar, J. Ping Liu. Adv. Mater. **23**, 821 (2011).

[3] Kang, J. General Purpose Permanent Magnet Motor Drive without Speed and Position Sensor, Yaskawa Electric Corp., Japan, Yaskawa Application Note WP.AFD.05.pdf

[4] J.M.D. Coey, Magnetism and Magnetic Materials. New York: Cambridge UP, 2009. Print.

[5] H. Zeng, J. Li, J.P. Liu, Z.L. Wang, S.H. Sun. Nature. **402**, 395 (2002).

[6] R.W. McCallum, L.H. Lewis, R. Skomski, M.J. Kramer, I.E. Anderson. Annu. Rev. Mater. Res. **44**, 451 (2014).

[7] S. Sugimoto, J. Phys. D: Appl. Phys. **44**, 064001(2011).

[8] "About the Size of a Watermelon, with a Lot More Juice". Tesla Motors, Inc. 2014. Web. 02 Dec. 2014.

[9] L. H. Lewis, A. Mubarok, E. Poirier, N. Bordeaux, P. Manchanda, A. Kashyap, R. Skomski, J. Goldstein, F. E. Pinkerton, R. K. Mishra, R. C. Kubic Jr, K. Barmak, J. Phys.: Condens. Matter **26,** 064213 (2014).

[10] E. Dos Santos, J. Gattacceca, P. Rochette, G. Fillion, R.B. Scorzelli, Journal of Magnetism and Magnetic Materials. **375**, 234 (2015).

[11] X. Guo, A. Zaluska, Z. Altounian and J. O. Ström-Olsen. Journal of Materials Research. **5**, 2646 (1990).

[12] J.B. Yang, W.B. Yelon, W.J. James, Q. Cai, M. Kornecki, S. Roy, N. Ali, P. L'Heritier, J. Phys. Condens. Matter. **14**, 6509 (2002).

[13] R. Coehoorn, R.A.Groot. J Phys. F: Met. Phys. **15**, 2135 (1985).

[14] L. J. Zhu, D. Pan, S. H. Nie, J. Lu, J. H. Zhao, Appl. Phys. Lett. **102**, 132403 (2013).

[15] H. Kurt, K. Rode, M. Venkatesan, P. Stamenov, J. M. D. Coey, physica status solidi (b). **248**, 2338 (2011).

[16] L. Zhu, J. Zhao, Applied Physics A. **111**, 379 (2013).

[17] L. Zhu, S. Nie, K. Meng, D. Pan, J. Zhao, H. Zheng, Advanced Materials. **24**, 4547 (2012).

[18] W.Y. Zhang, X.Z. Li, S.R. Valloppilly, R. Skomski, J.E. Shield, D.J. Sellmyer. J. Phys D: Appl. Phys. **46**, 135004 (2013).

[19] G.V. Ivanova, N.N. Shchegoleva, A.M. Gabay, Journal of Alloys and Compounds. **432**, 135 (2007).

[20] A.M. Gabay, Y. Zhang, G.C. Hadjipanayis, Journal of Magnetism and Magnetic Materials. **236**, 37 (2001).

[21] W. Zhang, S. R. Valloppilly, X. Li, R. Skomski, J. E. Shield, D. J. Sellmyer, IEEE Trans. Magn. **48**, 3603 (2012).

[22] M.C. Nguyen, K. Liqin, Z. Xin, V. Antropov, W. Cai-Zhuang, H. Kai-Ming, IEEE Trans. Magn. **48**, 3281 (2012).

[23] B. Balamurugan, B. Das, V. R. Shah, R. Skomski, X. Z. Li, D.J. Sellmyer, Appl. Phys. Lett. **101**, 122407 (2012).

[24] B. Das, B. Balamurugan, P. Kumar, R. Skomski, V.T. Shah, J.E. Shield, A. Kasyap, D.J. Sellmyer, IEEE Trans. Magn. **49**, 3330 (2013).

[25] K.H.J. Brschow, J. Appl. Phys. **53**, 7713 (1982).

[26] B. G. Demczyk, S. F. Cheng, J. Appl. Cryst. **24**, 1023 (1991).

[27] B. Balamurugan, B. Das, W.Y. Zhang, R. Skomski, D.J. Sellmyer, J. Phys.: Condens. Matter. **26**, 064204 (2014).

[28] V. K. Pecharsky and P.Y. Zavalij, Fundamentals of Powder Diffraction and Structural Characterization of Materials. New York: Springer, 2009

[29] D.Henry, N.Eby, J. Goodge, D. Mogk, "X-ray reflection in accordance with Bragg's Law". Carleton College 2012.

[30] B.D. Cullity and S.R. Stock, Elements of X-Ray Diffraction. New Jersey: Prentice-Hall, 2001.

[31] D.B. Willaims and C.B. Carter, Transmission Electron Microscopy. New York: Springer, 2009.

[32] J. Schweitzer, "Scanning Electron Microscope". Purdue University 2014.

[33] "The Transmission Electron Microscope". Nobelprize.org. Nobel Media AB 2014. Web.

[34] R. Skomski and J. M. D. Coey, Permanent Magnetism. Bristol: Institute of Physics Publishing, 1999.

[35] R. Skomski, P. Manchanda, P. Kumar, B. Balamurugan, A. Kashyap, D.J. Sellmyer, IEEE Trans. Magn. **49**, 3215, (2013).

[36] T.B. Massalski, Binary Alloy Phase Diagrams. Second Edition. Volume 1. ASM International, 1990.

[37] M. Ellner, Journal of Alloys and Compounds. **422**, 192 (2006).

[38] P. Manchanda, P. Kumar, A. Kashyap, M.J. Lucis, J.E. Shield, A.Mubarok , J. I. Goldstein , S. Constantinides , K. Barmak , L.H. Lewis , D. J. Sellmyer , R. Skomski, IEEE Trans, Magn. **49**, 5194 (2013).

[39] Q. Zeng, I. Baker, J.B. Cui, Z.C. Yan, Journal of Magnetism and Magnetic Materials. **308**, 214 (2007).

[40] E. Fazakas, L.K. Varga, F. Mazaleyrat, Journal of Alloys and Compounds. **434**, 611 (2007).

[41] S. Kojima, K. Kojima, S. Mitani, United States Patent No . 4133703 (17 August , 1977).

[42] E. Ma and M. Atzmon, Mater. Chem. and Phys. **39**, 249 (1995).

[43] Y. Geng, unpublished

[44] N. Poudyal, C. Rong, J. Ping Liu, J. of Appl. Phys. **107,** 09A703 (2010).

[45] N. Poudyal, V. Nguyen, C. Rong, J. Ping Liu. J of Phys. D: Appl. Phys. **44**, 335002 (2011).

[46] N. Akdogan. G. Hadjipanayis. D. Sellmyer. Nanotechnology. **21**, 295705 (2010).

[47]] K.P. Su, Z.W. Liu, D.C. Zeng, D.X. Huo, L.W. Li, G.Q. Zhang. J. of Phys. D. Appl. Phys. **46**, 245003 (2013).

[48] B.Z. Cui, L.Y. Zheng, W.F. Li, J.F. Liu, G.C. Hadjipanayis. Acta Materialia. **60**, 1721 (2012).

[49] M.J. Lucis, T.E. Prost, X. Jiang, M. Wang, J.E. Shield, Metals. **4**, 130 (2014).

 [50] H.M. Lu, W.T. Zheng, Q. Jiang, J. Phys. D: Appl. Phys. **40**, 320 (2007).

[51] "Calculated Co-Zr phase diagram". National Physics Laboratory 2011. Web.

[52] Q. Zeng, I. Baker, Z. Yan, Journal of Applied Physics. **99**, 08E902 (2006).

[53] C. Yanar, J.M.K. Wiezorek, V. Radmilovic, W.A. Soffa, Metallurgical and Materials Transactions A. **33**, 2413 (2002).

[54] Z.W. Liu, C. Chen, Z.G. Zheng, B.H. Tan, R.V. Ramanujan, J Mater Sci. **47**, 2333 (2012).

[55] H.X. Wang, P.Z. Si, W. Jiang, J.J. Liu, J.G. Lee, C.J. Choi, H.L. Ge, Advanced Materials Research. **287**, 1492 (2011).